Validation of a simple method for representing spheres and slender bodies in an immersed boundary method for Stokes flow on an unbounded domain

Thomas T. Bringley *, Charles S. Peskin

Courant Institute of Mathematical Sciences, New York University, 251 Mercer Street, New York, NY 10012, United States

Abstract

We test the efficacy of using a single Lagrangian point to represent a sphere, and a one-dimensional array of such points to represent a slender body, in a new immersed boundary method for Stokes flow. A numerical parameter, the spacing of the Eulerian grid, is used to determine the effective radius of the immersed sphere or slender body. Such representations are much less expensive computationally than those with two or three-dimensional meshes of Lagrangian points. To perform this test, we develop a numerical method to solve the discretized Stokes equations on an *unbounded* Eulerian grid which contains an arbitrary configuration of Lagrangian points that apply force to the fluid and that move with the fluid. We compare results computed with this new immersed boundary method to known results for spheres and rigid cylinders in Stokes flow in $\mathbb{R}^3$. We find that, for certain choices of parameters, the interactions with the fluid of a single Lagrangian point accurately replicate those of a sphere of some particular radius, independent of the location of the point with respect to the Eulerian grid. The interactions of a linear array of Lagrangian points, for certain choices of parameters, accurately replicate those of a cylinder of some particular radius, independent of the position and orientation of the array with respect to the Eulerian grid. The effective radius of the sphere and the effective radius of the cylinder turn out to be related in a simple and natural way. Our results suggest recipes for choosing parameters that should be useful to practitioners. One surprising result is that one must not use too many Lagrangian points in an array. Another is that the approximate delta functions traditionally used in the immersed boundary method perform much better than higher order delta functions with the same support.
© 2008 Elsevier Inc. All rights reserved.

Keywords: Immersed boundary method; Stokes equations; Slender-body theory; Numerical methods

1. Introduction

In numerical computations it is tempting, but dangerous, to use numerical parameters (such as grid spacing) for the representation of physical quantities (such as the radius of an immersed elastic filament). In this

---

* Corresponding author. Tel.: +1 212 998 3302; fax: +1 212 995 4121.
  E-mail addresses: bringley@cims.nyu.edu (T.T. Bringley), peskin@cims.nyu.edu (C.S. Peskin).

paper, we validate such a procedure for the immersed boundary method as applied to slender bodies and spheres in a Stokes fluid. Another contribution of the present paper is that we solve the Stokes equations in the presence of immersed bodies on an *unbounded* domain. This is particularly important at zero Reynolds number because of the long-range character of interactions in Stokes flow.

The immersed boundary method has been used to simulate diverse systems involving the interaction of fluid and elastic structure [1–6]. Recently, the method has been used for modeling cellular and sub-cellular biological processes that occur at very low Reynolds number [7–10]. Many such applications contain objects that might be represented as slender bodies or particles immersed in fluid. Examples of slender bodies include the tails of spermatozoa, eukaryotic cilia, bacterial flagella, microtubules, chromosomes, and strands of DNA and RNA. Objects such as cells, cell organelles, and individual protein molecules might, at a low level of detail, be represented as spherical particles. Outside biology, the immersed boundary method has been used in studying particle and filament suspensions at low Reynolds number [11–13]. At larger scales, fibers are the basic constituents of many biological tissues, and many higher Reynolds number immersed boundary method computations involve elastic structures that are constructed of fibers [4].

Slender bodies in the immersed boundary method have often been represented in a particularly simple way. Instead of using a two- or three-dimensional mesh of Lagrangian immersed boundary points to define the position of the body, a linear array of points is used [10,14,15]. In practice, this is what is meant when it is said that a body is constructed of fibers. Particles, in some applications, have been represented as a single immersed boundary point [11,16]. Moreover, single immersed boundary points have often been used to visualize flow in the immersed boundary method.

There is a vast computational savings associated with using these simple representations of spheres and slender bodies. Many fewer immersed boundary points are needed to represent a body, the configuration of points is simple, and, for slender bodies, it is easy to specify arbitrary elastic behavior in response to stretching and bending. Also, the spacing of the Eulerian fluid grid is typically on the order of the spacing of the Lagrangian mesh, so using a complicated mesh requires refining the fluid grid significantly. The time step must then be reduced accordingly. In three dimensions, this refinement is exceedingly costly. Moreover, a complicated Lagrangian mesh is likely to introduce extra stiffness constraints that require even a further reduction in the time step.

Some questions may arise about the approach of using these simple representations. If a single immersed boundary point is meant to represent a sphere, what is sphere's radius? What is the radius of a slender body represented by a one-dimensional array of immersed boundary points? How many points should be used? Finally, is this method accurate and consistent as the immersed boundary points change their position and, in the case of a slender body, their collective orientation relative to the Eulerian fluid grid?

In this paper, we attempt to answer these questions. We focus on the case of zero Reynolds number because many interesting applications occur in this regime and because results from slender-body theory are available for comparison. We first develop a numerical method in Section 2 to solve the Stokes equations on an infinite three-dimensional grid. We do this by calculating the Green's function for the discretized equations. Coupling this calculation to the immersed boundary method allows us to calculate the linear relationship between the forces that a given configuration of immersed boundary points apply to the fluid and the resulting velocities of those points. We formulate our method for rigid bodies, though it could be used for bodies that can change shape. Rigid bodies pose the additional problem that a constraint force must arise to maintain the body's rigidity. We calculate the resistance matrix of the body, which gives the linear relationship between the translational and rotational velocities of the body and the forces and torques applied. We are also able to calculate the velocity at any point in the fluid grid created by the motion of the body.

In Section 3, we use this method to study the interaction with the fluid of a single Lagrangian point to which an external force is applied. We compare the computed results to the exact solution for Stokes flow around a sphere. We show that, for certain choices of the approximate delta function used in the immersed boundary method, the resistance matrix is close to that of a sphere of some particular radius and is essentially independent of the location of the Lagrangian point with respect to the Eulerian grid. We call the radius of this sphere the effective radius of an immersed boundary point. We also calculate the velocity field generated by a translating point and show that it is close to that created by a translating sphere whose radius is the effective radius.

In Section 4, we study the interaction with the fluid of a linear array of Lagrangian points that are constrained to move as a rigid body, and we compare results to those of slender-body theory for a rigid cylinder. We show that there is a range of preferred densities of immersed boundary points relative to the Eulerian grid spacing. At these densities the interactions of the Lagrangian array with the fluid are essentially independent of the position and orientation of the array relative to the Eulerian grid. Also, the resistance matrix of such an array is close to that of the slender-body theory approximation for a rigid cylinder of some effective radius. Given the effective radius of a sphere represented by a single immersed boundary point, we determine the effective radius of the cylinder by a mathematical argument, and do so without fitting parameters. We show that the computed and slender-body velocity fields in the fluid are in good agreement as well.

We conclude that simple representations of spheres and rigid cylinders in the immersed boundary method can be used with only a small loss of accuracy and with large computational savings. Our results suggest that this conclusion will hold for slender bodies with curvature or which are non-rigid. Moreover, we identify values of the relevant parameters, such as the effective radius of an immersed boundary point and the effective radius and length of an array of points. The radii are proportional to the Eulerian grid spacing, so this grid spacing can be chosen so as to represent a sphere or cylinder of arbitrary radius. Spheres and cylinders of several different radii may be represented simultaneously if several different approximate delta functions are used.

In principle, our numerical method works for an arbitrary discretization of the Stokes equations, and we investigate both a second-order finite difference discretization and a spectral discretization. We find that these two discretizations give nearly identical qualitative results and very similar quantitative results. Our method also makes sense for an arbitrary choice of the approximate delta function. We investigate a variety of delta functions, and find that the delta functions conventionally used in the immersed boundary method give superior performance when compared to higher order delta functions of the same support. In particular, the sensitivity of results to position and orientation relative to the grid is much smaller when the conventional immersed boundary delta functions are used.

2. An immersed boundary method for Stokes flow in an unbounded domain with rigid bodies

2.1. The continuous immersed boundary method

We begin with a brief description of the immersed boundary method for Stokes flow. A more detailed description of the immersed boundary method can be found in Ref. [4]. The method is formulated first as a system of partial differential equations in continuous variables, which we shall later discretize. Consider a solid body immersed in a viscous fluid in three dimensions. This method could easily be generalized to the case of multiple bodies.

In typical immersed boundary method computations, the fluid occupies a finite box. One purpose of this paper is to find a means of dealing with the unbounded case. We therefore assume that the domain occupied by the fluid and body together is $\mathbb{R}^3$. Boundaries have long-range effects in the Stokes equations, and eliminating them allows us to isolate the fluid–body interactions. For instance, in an infinite fluid, symmetry dictates that the drag on a sphere should not depend on the sphere's position or the direction in which it moves. We test whether this is true in the discrete immersed boundary method. Also, using an infinite fluid allows us to compare our results with the exact solution for a sphere in an infinite fluid and approximate solutions for a finite rigid cylinder in an infinite fluid derived from slender-body theory. We take the fluid to be at rest at infinity.

The immersed boundary method uses both Eulerian and Lagrangian coordinates. The Eulerian description applies both to the fluid and to the solid body. Lagrangian coordinates are needed only for the body. We first state the Eulerian equations.

At zero Reynolds number, the fluid obeys the Stokes equations. In the immersed boundary method, the Stokes equations are taken to hold in all of space, including that occupied by the body. These equations are

$$\nabla p = \mu \Delta \mathbf{u} + \mathbf{f} \tag{1}$$
$$\nabla \cdot \mathbf{u} = 0 \tag{2}$$

The parameter μ is the viscosity of the fluid, $\mathbf{u}$ is the Eulerian velocity, p is the pressure, and $\mathbf{f}$ is an Eulerian force density applied by the immersed body to the fluid, which will be specified later. All quantities in Eqs. (1) and (2) are functions of the Eulerian variable $\mathbf{x}$. The boundary conditions, assuming the solid body is finite, are that $\mathbf{u}$ and $\mathbf{p}$ approach zero as $|\mathbf{x}|$ approaches infinity. The fluid obeys the no-slip condition on the surface of the body, which means that $\mathbf{u}$ is continuous at the body-fluid interface.

That these equations hold everywhere is motivated by the many biological applications in which fluid actually does permeate tissue. However, even in cases where the fluid is separate, the Stokes equations are the correct Eulerian equations for a rigid body or an incompressible elastic body whose motion is highly damped by viscosity, provided $\mathbf{f}$ is chosen appropriately. We consider rigid bodies, inside which the Laplacian of $\mathbf{u}$ is zero, so we may take μ to be independent of $\mathbf{x}$.

We now state the Lagrangian equations. The configuration of the solid body is denoted by $\mathbf{X}$. The velocity is $\mathbf{U}$. Both are functions of the Lagrangian coordinate $\mathbf{q}$ which takes values in the set Ω. The equation of motion is

$$\mathbf{X}(\mathbf{q})_t = \mathbf{U}(\mathbf{q}) \tag{3}$$

where the subscript t denotes partial differentiation with respect to time.

The Lagrangian force density applied by the solid body is denoted by $\mathbf{F}$. For an elastic body, $\mathbf{F}$ is taken to be some function of the body's configuration. For a rigid body, $\mathbf{F}$ is the sum of a known force density that is applied to the body, $\mathbf{F}^a$, and an unknown force density that maintains the body's rigidity, $\mathbf{F}^c$, called the constraint force density. We consider rigid bodies and study their motion as a function of $\mathbf{F}^a$. The constraint force density, to be consistent with conservation of momentum and angular momentum, must apply no net force or torque.

$$\int_\Omega \mathbf{F}^c(\mathbf{q})\mathbf{dq} = 0 \tag{4}$$

$$\int_\Omega \mathbf{X}(\mathbf{q}) \times \mathbf{F}^c(\mathbf{q})\mathbf{dq} = 0 \tag{5}$$

In the continuous system, there may be many $\mathbf{F}^c$ that both satisfy these equations and maintain the rigidity of the body. The choice, however, will not affect the motion of the body or the fluid. In the discretized systems that we consider, there will be a unique choice of $\mathbf{F}^c$.

We now describe how the Eulerian variables interact with the Lagrangian variables. Two statements are needed. The first is that the Eulerian velocity $\mathbf{u}$ and Lagrangian velocity $\mathbf{U}$ are equal at corresponding points. The second is that the Eulerian force density $\mathbf{f}$ and Lagrangian force density $\mathbf{F}$ are, at corresponding points, equal as densities, meaning they are equal if integrated over corresponding regions of $\mathbf{x}$ and $\mathbf{q}$ space. The functions themselves are not equal in general but can be made equal if one is multiplied by the appropriate Jacobian. One way to express these statements that will prove convenient is by integrals against a Dirac delta function.

$$\mathbf{U}(\mathbf{q}) = \int_{\mathbb{R}^3} \mathbf{u}(\mathbf{x})\delta(\mathbf{x} - \mathbf{X}(\mathbf{q}))\mathbf{dx} \tag{6}$$

$$\mathbf{f}(\mathbf{x}) = \int_\Omega \mathbf{F}(\mathbf{q})\delta(\mathbf{x} - \mathbf{X}(\mathbf{q}))\mathbf{dq} \tag{7}$$

The Stokes equations (1) and (2), the kinematic equation for the solid body, (3), and the two interaction equations (6) and (7), along with a specification of how $\mathbf{F}$ is determined constitute the complete continuous system. We now describe the solution of this system and some of its properties. We show later that the discretized system has analogous properties.

The Stokes equations are linear and have constant coefficients, so they have a Green's function known at the Stokeslet, $\mathcal{S}_0$.

$$\mathcal{S}_0(\mathbf{x}) = \frac{1}{8\pi\mu}\frac{\mathcal{I} + \hat{\mathbf{x}}\hat{\mathbf{x}}^T}{|\mathbf{x}|} \tag{8}$$

The symbol $\mathcal{I}$ denotes the 3×3 identity matrix. The variable $\hat{\mathbf{x}} = \mathbf{x}/|\mathbf{x}|$. The Stokeslet is matrix valued because, for each $\mathbf{x}$, it is the linear transformation from the force at the origin to the velocity at $\mathbf{x}$. Given $\mathbf{f}$, we can solve for $\mathbf{u}$

$$\mathbf{u}(\mathbf{x}) = \int_{\mathbb{R}^3} \mathcal{S}_0(\mathbf{x} - \mathbf{x}')\mathbf{f}(\mathbf{x}')\mathbf{dx}' \tag{9}$$

Combining Eq. (9) with the interaction equations (6) and (7), gives a Green's function, $\mathcal{G}_0$, relating the Lagrangian variables $\mathbf{F}$ and $\mathbf{U}$.

$$\mathcal{G}_0(\mathbf{q}, \mathbf{q}') = \int \int_{\mathbb{R}^6} \delta(\mathbf{x} - \mathbf{X}(\mathbf{q}))\mathcal{S}_0(\mathbf{x} - \mathbf{x}')\delta(\mathbf{x}' - \mathbf{X}(\mathbf{q}'))\mathbf{dx}\,\mathbf{dx}' \tag{10}$$

$$\mathbf{U}(\mathbf{q}) = \int_{\Omega} \mathcal{G}_0(\mathbf{q}, \mathbf{q}')\mathbf{F}(\mathbf{q}')\mathbf{dq}' \tag{11}$$

A convenient property of the Stokeslet is its scaling behavior

$$\mathcal{S}_0(\mathbf{x}) = \lambda\mathcal{S}_0(\lambda\mathbf{x}) \tag{12}$$

If $\mathbf{X}' = \lambda\mathbf{X}$, this scaling is inherited by the the Lagrangian Green's function

$$\mathcal{G}_0(\mathbf{q}, \mathbf{q}') = \lambda\mathcal{G}_0'(\mathbf{q}, \mathbf{q}') \tag{13}$$

Another convenient property of the Stokeslet is its Fourier space representation, obtained by solving the Stokes equations using the Fourier transform

$$\mathcal{S}_0(\mathbf{x}) = \int_{\mathbb{R}^3} \frac{1}{4\pi^2\mu|\mathbf{k}|^2}(\mathcal{I} - \hat{\mathbf{k}}\hat{\mathbf{k}}^{\mathrm{T}})\mathrm{e}^{2\pi i\mathbf{k}\cdot\mathbf{x}}\,\mathbf{dk} \tag{14}$$

2.2. The discrete immersed boundary method

We discretize the Stokes equations on an *infinite* Eulerian grid with uniform grid-spacing h

$$\mathbf{D}_h p = \mu L_h \mathbf{u} + \mathbf{f} \tag{15}$$

$$\mathbf{D}_h \cdot \mathbf{u} = 0 \tag{16}$$

The variables $\mathbf{u}$, p, and $\mathbf{f}$ are now defined on the grid. The discrete divergence operator for functions on the grid is denoted by $\mathbf{D}_h$, and the discrete Laplacian operator by L_h. The exact choices of $\mathbf{D}_h$ and L_h do not affect how we solve the system, provided they satisfy reasonable assumptions. In our computations, we use two different choices so that we can check if our results depend on the discretization method used. One choice uses the second-order centered finite difference operator for the gradient, $\mathbf{D}^{\mathrm{f}}_h$, and the second-order seven-point finite difference discretization of the Laplacian, L^{f}_h. The other choice uses spectral differentiation for the gradient, $\mathbf{D}^{\mathrm{s}}_h$, and the spectral Laplacian, L^{s}_h. The boundary conditions continue to be that $\mathbf{u}$ and p approach zero as $|\mathbf{x}|$ approaches infinity. The no-slip condition at the solid-fluid boundary will be satisfied automatically, though only approximately, because the viscous term in Eq. (15) couples the velocity at nearby grid cells. As we shall see, the velocity of the discrete representation of the body will be interpolated from nearby fluid grid points, so the body will move at approximately the local fluid velocity. One goal of this paper is to test how well the no-slip condition is satisfied for some very simple immersed bodies.

The solid body is discretized into a Lagrangian mesh of what we call immersed boundary points. The variable $\mathbf{q}$ is now an element of a finite index set, Ω. The position of an immersed boundary point, $\mathbf{X}(\mathbf{q})$, need not be a point on the Eulerian grid. In this paper, we are concerned only with relationship between force and velocity for a solid body at a single moment, not with the dynamical evolution of the body's configuration, so we do not need to specify a discretization in time of Eq. (3).

To simplify the notation, we let $\mathbf{F}$ be the total force applied by the immersed boundary point $\mathbf{q}$ instead of the force density. Still, $\mathbf{F}$ is the sum of $\mathbf{F}^{\mathrm{a}}$ and $\mathbf{F}^{\mathrm{c}}$. The applied force, $\mathbf{F}^{\mathrm{a}}$, is a specified function of $\mathbf{q}$. We later show that, for our particular configurations of immersed boundary points, the constraint force $\mathbf{F}^{\mathrm{c}}$ is uniquely determined.

In general, the immersed boundary points will not lie on the Eulerian grid, so there is no trivial notion of the Eulerian velocities, **u**, and Lagrangian velocities, **U**, being equal at corresponding points. Instead, the Lagrangian velocities are interpolated from the Eulerian grid by an approximate Dirac delta function, δ_h. Similarly, the Lagrangian force **F** is spread to the Eulerian grid by δ_h, producing the Eulerian force density **f**

$$\mathbf{U}(\mathbf{q}) = \sum_{\mathbf{x} \in (h\mathbb{Z})^3} \mathbf{u}(\mathbf{x}) \delta_h(\mathbf{x} - \mathbf{X}(\mathbf{q})) h^3 \tag{17}$$

$$\mathbf{f}(\mathbf{x}) = \sum_{\mathbf{q} \in \Omega} \mathbf{F}(\mathbf{q}) \delta_h(\mathbf{x} - \mathbf{X}(\mathbf{q})) \tag{18}$$

In this paper, we test the performance of a variety of approximate delta functions. We classify the delta functions that we use into three families, based on how the functions are constructed. It is essential, for our method, that a delta function have a small support, and each family contains a hierarchy of delta functions of increasingly broad support. Now, we briefly describe the construction of these functions and introduce our notation. Formulas for all the functions used in this paper, as well as plots, can be found in the Appendix.

In all cases, we assume that the three-dimensional delta functions are products of one-dimensional functions,

$$\delta_h(\mathbf{x}) = \frac{1}{h^3} \phi(x/h) \phi(y/h) \phi(z/h), \tag{19}$$

where $\mathbf{x} = (x, y, z)$. A delta function is constructed by imposing enough conditions on ϕ so that it is uniquely determined. These conditions include that the delta function provides a specified order of interpolation. It can be shown that a delta function will provide order of interpolation m if and only if the following discrete moment conditions are satisfied by ϕ [17]:

$$\sum_{j \in \mathbb{Z}} \phi(x - j) = 1 \quad \forall x \in \mathbb{R} \tag{20}$$

$$\sum_{j \in \mathbb{Z}} (x - j)^k \phi(x - j) = 0 \quad \forall x \in \mathbb{R}, \quad 1 \leqslant k \leqslant m - 1. \tag{21}$$

For ϕ to be continuous, which we require, it so happens that the interpolation order must be an even integer.

For some functions we also impose what is called the sum of squares condition:

$$\sum_{j \in \mathbb{Z}} \phi(x - j)^2 = \sum_{j \in \mathbb{Z}} \phi(j)^2 \quad \forall x \in \mathbb{R}. \tag{22}$$

Finally, for some functions we impose what we call the balanced condition:

$$\sum_{j \in \mathbb{Z} \text{ even}} \phi(x - j) = \sum_{j \in \mathbb{Z} \text{ odd}} \phi(x - j) \quad \forall x \in \mathbb{R}. \tag{23}$$

Motivation of these two conditions can be found in Ref. [4]. The delta functions themselves will satisfy a sum of squares or balanced condition in three dimensions if the one-dimensional functions ϕ satisfy these conditions.

The first family of delta functions we consider satisfy neither the sum or squares nor the balanced condition. Instead, they provide the maximum possible order of interpolation [17]. We denote these functions by $\delta_{d,h}^{\mathrm{M}}$. The index d is an even integer which indicates the support width of the delta function in units of h. The order of interpolation is d. The superscript M is meant to stand for "maximum moment conditions". In this paper, we use the functions $\delta_{2,h}^{\mathrm{M}}$, $\delta_{4,h}^{\mathrm{M}}$, and $\delta_{6,h}^{\mathrm{M}}$.

The second family of delta functions we consider satisfy the sum of squares conditions but not the balanced condition. We denote these functions by $\delta_{d,h}^{\mathrm{IB}}$, where d is an odd integer which indicates the function's support width. These functions have interpolation order $d - 1$. In this paper, we use the functions $\delta_{3,h}^{\mathrm{IB}}$ and $\delta_{5,h}^{\mathrm{IB}}$. The third family of delta functions satisfy both the sum of squares and the balanced condition. We also denote these functions by $\delta_{d,h}^{\mathrm{IB}}$, where d is an even integer (so there is no ambiguity) which indicates the support width. These functions have interpolation order $d - 2$. In this paper, we use the functions $\delta_{4,h}^{\mathrm{IB}}$ and $\delta_{6,h}^{\mathrm{IB}}$.

We use the superscript IB because the immersed boundary method has traditionally used delta functions which satisfy the sum of squares condition. The standard delta function for immersed boundary method computations is $\delta_{4,h}^{\mathrm{IB}}$, and it is described in detail in Ref. [4]. The function $\delta_{3,h}^{\mathrm{IB}}$ was first used in Ref. [18], and higher order versions of these functions were introduced in Ref. [19].

Any delta function may be dilated by a positive integer if also scaled appropriately to create a new delta function which provides the same interpolation order and satisfies the same conditions. In this paper, we use one such function which we denote by $\delta_{4,h}^{\mathrm{D}}$. It is obtained by dilating $\delta_{2,h}^{\mathrm{M}}$ by 2 and scaling by 1/8. The superscript D is meant to stand for "dilated". Later in this paper we set h to one and drop the h subscript from all delta functions.

The discrete Stokes equations (15) and (16), the kinematic Eq. (3), and the discrete interaction equations (17) and (18), along with a specification of how **F** is determined, constitute the complete discretized system. We now describe the solution of this system.

The discrete Stokes equations are linear difference equations with constant coefficients, so a Green's function must exist. This function, which we refer to as the discrete Stokeslet, $\mathcal{S}_h$, allows us to solve for **u** in terms of **f**.

$$\mathbf{u}(\mathbf{x}) = \sum_{\mathbf{x}' \in (h\mathbb{Z})^3} \mathcal{S}_h(\mathbf{x} - \mathbf{x}')\mathbf{f}(\mathbf{x}')h^3 \tag{24}$$

Finding $\mathcal{S}_h$ requires solving an elliptic difference equation on an infinite grid, a seemingly difficult task. However, as in the case of Eq. (14) for the Stokeslet, we can find a Fourier space representation of the discrete Stokeslet by taking the Fourier transform of the difference equations

$$\mathcal{S}_h(\mathbf{x}) = \frac{1}{h\mu} \int_{[-\frac{1}{2},\frac{1}{2}]^3} \frac{1}{\alpha(\mathbf{k})} (\mathcal{I} - \hat{\mathbf{g}}(\mathbf{k})\hat{\mathbf{g}}(\mathbf{k})^{\mathrm{T}})\mathrm{e}^{2\pi i \mathbf{k} \cdot \mathbf{x}/h} \, \mathbf{dk} \tag{25}$$

The functions α and **g** depend on which discretization method is used for the Stokes equations. For the finite difference discretization

$$\alpha^{\mathrm{f}}(\mathbf{k}) = 4|\sin(\pi\mathbf{k})|^2, \quad \mathbf{g}^{\mathrm{f}}(\mathbf{k}) = \sin(2\pi\mathbf{k}). \tag{26}$$

For the spectral discretization

$$\alpha^{\mathrm{s}}(\mathbf{k}) = 4\pi^2|\mathbf{k}|^2, \quad \mathbf{g}^{\mathrm{s}}(\mathbf{k}) = \mathbf{k}. \tag{27}$$

These agree to second-order when $|\mathbf{k}|$ is small.

The discrete Stokeslet is a real symmetric 3×3 matrix valued function of **x**, which takes values on the infinite Eulerian grid. The integral in Eq. (25) converges absolutely for any consistent discretization of the Stokes equations, though there is a singularity of degree two at the origin.

We compute these integrals by numerical quadrature. Several observations simplify this task. First, we make use of the scaling behavior of the discrete Stokeslet to express $\mathcal{S}_h$ in terms of $\mathcal{S}_1$

$$\mathcal{S}_1(\mathbf{x}) = h\mathcal{S}_h(h\mathbf{x}) \tag{28}$$

We need only calculate the Stokeslet for $h = 1$. All of our results scale with h in a simple way, so we set $h = 1$ for the remainder of this paper. Similarly, $\mathcal{S}_h$ is inversely proportional to μ, and all results scale with μ in a simple way. We thus set $\mu = 1$.

Second, we make use of the symmetries of $\mathcal{S}_1$, which we briefly state. If s_1, s_2, and s_3 are ± 1, then the (i,j)th component of $\mathcal{S}_1(s_1 x, s_2 y, s_3 z)$ equals the (i,j)th component of $s_i s_j \mathcal{S}_1(x, y, z)$. Now, if s_1, s_2, and s_3 are a permutation of the numbers 1, 2, and 3, and if $\mathbf{x}_s$ is the vector whose ith component is $\mathbf{x}_{s_i}$, then the (i,j)th component of $\mathcal{S}_1(\mathbf{x}_s)$ is the (s_i, s_j)th component of $\mathcal{S}_1(\mathbf{x})$. From these we deduce that we need only compute $\mathcal{S}(\mathbf{x})$ for **x** having non-negative components whose values are non-increasing. Finally, we can reduce the integration domain to $[0, 1/2]^3$ and can eliminate the need for complex numbers by using the oddness and evenness properties of the integrand in Eq. (25).

Each integral is computed using a specialized quadrature method. We use a smooth partition of unity to isolate the singularity at the origin and also, for the finite difference discretization, the discontinuity singular-

ities that occur at the other corners of the integration domain. The singular integrals are computed in spherical coordinates, which removes their singularities, using four point Gauss–Legendre quadrature. The remaining integral to be computed is highly oscillatory when $|\mathbf{x}|$ is large, so we use a specialized method for computing oscillatory integrals due to Ixaru and Paternoster [20]. Their method provides quadrature weights and abscissae so that functions of the form $k^n \exp(\pm 2\pi i \omega k)$ are integrated exactly for $n = 0, \ldots, p$ and for fixed ω. We use $p = 3$.

If we need values of $\mathcal{S}_1(\mathbf{x})$ for $\mathbf{x}$ taking integral values between $-M$ and M, we must compute approximately $M^3/6$ integrals, each having six components. For this paper, we have used $M = 60$. Convergence studies indicate that our quadrature method is converging quickly, and we claim that our computed values of $\mathcal{S}_1$ have at least six digits of accuracy. We only have to compute these integrals once, and we have tabulated their values for later use.

Combining the discrete interaction equations (17 and 18), with the equation relating the Eulerian force density and velocity (24), we find an equation describing the relationship between the Lagrangian force applied by the immersed boundary points and velocity of the points.

$$\mathcal{G}_1(\mathbf{q}, \mathbf{q}') = \sum_{\mathbf{x}, \mathbf{x}' \in \mathbb{Z}^3} \delta_1(\mathbf{x} - \mathbf{X}(\mathbf{q})) \mathcal{S}_1(\mathbf{x} - \mathbf{x}') \delta_1(\mathbf{x}' - \mathbf{X}(\mathbf{q}')) \tag{29}$$

$$\mathbf{U}(\mathbf{q}) = \sum_{\mathbf{q}' \in \Omega} \mathcal{G}_1(\mathbf{q}, \mathbf{q}') \mathbf{F}(\mathbf{q}') \tag{30}$$

The linear relationship between $\mathbf{F}$ and $\mathbf{U}$ is given by $\mathcal{G}_1$, the discrete Green's function for the Lagrangian variables. If there are N immersed boundary points, $\mathcal{G}_1$ is an $N \times N$ array of 3×3 matrices. Each 3×3 matrix is symmetric, and $\mathcal{G}_1$ is symmetric in $\mathbf{q}$ and $\mathbf{q}'$.

An interesting fact is that because we use approximate delta functions of the form shown in Eq. (19), the matrix $\mathcal{G}(\mathbf{q}, \mathbf{q})$, which describes the self-induced velocity of an immersed boundary point, is always exactly diagonal. To see why, first note that $\delta(\mathbf{x} - \mathbf{X}(\mathbf{q}))\delta(\mathbf{x}' - \mathbf{X}(\mathbf{q}))$ does not change if $\mathbf{x}$ and $\mathbf{x}'$ exchange one of their components (because of Eq. (19)). Second, note that the (i,j)th off-diagonal element of $\mathcal{S}_1(\mathbf{x} - \mathbf{x}')$ does change sign if $\mathbf{x}$ and $\mathbf{x}'$ exchange their ith (or jth) component. Finally, note that the (i,j)th off-diagonal element of $\mathcal{S}_1(\mathbf{x})$ is zero if the ith (or jth) component of $\mathbf{x}$ is zero. These facts imply that the off-diagonal components of the summands in Eq. (29) are either zero or cancel pairwise when $\mathbf{q} = \mathbf{q}'$.

If the approximate delta functions have finite support, the sum in Eq. (29) has finitely many non-zero terms. Thus, $\mathcal{G}_1$ may be computed provided we have tabulated all necessary values of $\mathcal{S}_1$. If the width of the support of the delta function is d, we need that the immersed boundary points are not, in any dimension, farther apart than $M - d - 1$ grid cells. For a large number of points, calculating $\mathcal{G}_1$ is computationally intensive. The complexity is of order N^2 in the number of points and d^6 in the width of the support of the delta function. Because of this sixth degree scaling, it is impractical to use a delta function whose support has width greater than six.

When h is not one, if the approximate delta function scales as in Eq. (19) and if the Lagrangian point configuration, $\mathbf{X}$, is scaled as $\mathbf{X}_1 = h\mathbf{X}_h$, then the discrete Green's function for the Lagrangian variables will inherit the scaling of the Stokeslet.

$$\mathcal{G}_1(\mathbf{q}, \mathbf{q}') = h\mathcal{G}_h(\mathbf{q}, \mathbf{q}') \tag{31}$$

2.3. Finding the constraint force

After $\mathcal{G}_1$ has been found for a particular configuration of immersed boundary points, the constraint force $\mathbf{F}^c$ that maintains the body's rigidity may be determined. To do this, we think of $\mathbf{U}$ and $\mathbf{F}$ as vectors in $\mathbb{R}^{3N}$, and we think of $\mathcal{G}_1$ as a $3N$ by $3N$ matrix.

For $\mathbf{U}$ to be a velocity of a rigid motion, it must lie in the six-dimensional space of translations and rotations which we shall call V. The elementary translations, $\mathbf{U} = \mathbf{e}_i$ for $i = 1, 2, 3$, where $\mathbf{e}_i$ is a standard basis element in $\mathbb{R}^3$, and the elementary rotations, $\mathbf{U} = \mathbf{e}_i \times (\mathbf{X}(\mathbf{q}) - \mathbf{X}_0)$ for $i = 1, 2, 3$, where $\mathbf{X}_0$ is the mean of $\mathbf{X}$, form a basis for V that we call the standard basis for V.

To be consistent with conservation of momentum and angular momentum, the constraint force must apply zero net force and torque

$$\sum_{\mathbf{q}\in\Omega}\mathbf{F}^{\mathrm{c}}(\mathbf{q}) = 0 \tag{32}$$

$$\sum_{\mathbf{q}\in\Omega}\mathbf{X}(\mathbf{q})\times\mathbf{F}^{\mathrm{c}}(\mathbf{q}) = 0 \tag{33}$$

These equations imply that $\mathbf{F}^{\mathrm{c}}$ is orthogonal to V. Choose arbitrary orthonormal bases for V and $V^{\perp}$, so that, together, they form a complete orthonormal basis for $\mathbb{R}^{3N}$. Order the basis elements such that the first $\dim(V)$ of them span V. We express the vectors $\mathbf{U}$, $\mathbf{F}^{\mathrm{a}}$ and $\mathbf{F}^{\mathrm{c}}$ in terms of this basis as

$$\mathbf{U} = \begin{pmatrix} \mathbf{U}_1 \\ 0 \end{pmatrix}, \quad \mathbf{F}^{\mathrm{a}} = \begin{pmatrix} \mathbf{F}_1^{\mathrm{a}} \\ \mathbf{F}_2^{\mathrm{a}} \end{pmatrix}, \quad \mathbf{F}^{\mathrm{c}} = \begin{pmatrix} 0 \\ \mathbf{F}_2^{\mathrm{c}} \end{pmatrix} \tag{34}$$

where vectors with subscript 1 have the same dimension as V and vectors with subscript 2 have dimension $3N - \dim(V)$. We also express $\mathcal{G}_1$ in this basis, and we write Eq. (30) in block form

$$\begin{pmatrix} \mathbf{U}_1 \\ 0 \end{pmatrix} = \begin{pmatrix} \mathcal{G}_1^{11} & (\mathcal{G}_1^{21})^{\mathrm{T}} \\ \mathcal{G}_1^{21} & \mathcal{G}_1^{22} \end{pmatrix} \left[\begin{pmatrix} \mathbf{F}_1^{\mathrm{a}} \\ \mathbf{F}_2^{\mathrm{a}} \end{pmatrix} + \begin{pmatrix} 0 \\ \mathbf{F}_2^{\mathrm{c}} \end{pmatrix} \right] \tag{35}$$

For there to be a unique solution for $\mathbf{F}^{\mathrm{c}}$, we must assume that $\mathcal{G}_1$ is invertible, which will be true if there are no non-trivial forces $\mathbf{F}$ that produce a velocity $\mathbf{U}$ that is identically zero. In the continuous case, even though the constraint force may not be uniquely defined, the motion of the body and the fluid is unique. In the discrete case, if $\mathcal{G}_1$ is not invertible, it is not clear that the motion would be unique. It is also not clear that the rigid body motions would even lie in the column space of $\mathcal{G}_1$.

Two specific types of problems can occur. In the continuous immersed boundary method, $\mathcal{G}_0$ is typically not invertible. For instance, a symmetric uniform inward-pointing force on a spherical shell will result in zero velocity because the incompressibility of the fluid creates an outward pressure to balance the force. In certain symmetric situations, a similar issue could arise in the discrete immersed boundary method. This does not happen when there is a single immersed boundary point or when the points are arranged in a line.

Another possible problem is that the rank of $\mathcal{G}_1$ is bounded above by the rank of the operator that spreads forces from the immersed boundary points to the grid. The rank of this operator is bounded above by three times the number of grid points that are no farther than the width of the support of the approximate delta function from the nearest immersed boundary point. If the immersed boundary points occupy N_{B} distinct grid boxes, and the width of the support of the delta function is d, then the rank of $\mathcal{G}_1$ is at most $3N_{\mathrm{B}}d^3$. If $N > N_{\mathrm{B}}d^3$, $\mathcal{G}_1$ cannot possibly be invertible. So, the density of immersed boundary points can be at most d^3 per grid box. Even if the density is smaller, $\mathcal{G}_1$ will become ill-conditioned as N becomes large. We see later that, for a cylinder, it is optimal to use far fewer points. At these optimal densities and for our configurations, we find that $\mathcal{G}_1$ is not only invertible, but has a reasonable condition number.

Solving the block system, the constraint force and the velocity can be found

$$\mathbf{F}_2^{\mathrm{c}} = -\mathbf{F}_2^{\mathrm{a}} - (\mathcal{G}_1^{22})^{-1}\mathcal{G}_1^{21}\mathbf{F}_1^{\mathrm{a}} \tag{36}$$

$$\mathbf{U}_1 = (\mathcal{G}_1^{11} - (\mathcal{G}_1^{21})^{\mathrm{T}}(\mathcal{G}_1^{22})^{-1}\mathcal{G}_1^{21})\mathbf{F}_1^{\mathrm{a}} \tag{37}$$

The velocity does not depend on $\mathbf{F}_2^{\mathrm{a}}$, so it only matters what total force and torque is applied to the immersed boundary points, not the higher moments of the force distribution. We wish to express the linear relationship between the total forces and torques applied to the body and the velocities and angular velocities of the body. Let $\mathcal{P}$ be the $3N \times 6$ matrix whose columns are the standard basis elements of V. The coordinates of $\mathbf{U}$ in this basis are the translational and rotational velocities of the body. We denote these by the vector $\mathcal{U}$ in $\mathbb{R}^6$, so that $\mathbf{U} = \mathcal{P}\mathcal{U}$. Let $\mathcal{F}$ be the vector in $\mathbb{R}^6$ whose components are the total forces and torques applied to the body. These components are dot products of the force with the standard basis elements of V so that $\mathcal{F} = \mathcal{P}^{\mathrm{T}}\mathbf{F}^{\mathrm{a}}$. The range of $\mathcal{P}$ is V, so $\mathcal{P}$ can be written in block form as

$$\mathcal{P} = \begin{pmatrix} \mathcal{P}_1 \\ 0 \end{pmatrix}. \tag{38}$$

Thus, $\mathbf{U}_1 = \mathcal{P}_1 \mathcal{U}$ and $\mathcal{F} = \mathcal{P}_1^{\mathrm{T}} \mathbf{F}_1^{\mathrm{a}}$. The linear relationship between $\mathcal{U}$ and $\mathcal{F}$ is then given by a 6×6 symmetric matrix called the resistance matrix, $\mathcal{R}$.

$$\mathcal{R} = \mathcal{P}_1^{\mathrm{T}} (\mathcal{G}_1^{11} - (\mathcal{G}_1^{21})^{\mathrm{T}} (\mathcal{G}_1^{22})^{-1} \mathcal{G}_1^{21})^{-1} \mathcal{P}_1 \tag{39}$$

$$\mathcal{F} = \mathcal{R} \mathcal{U} \tag{40}$$

It is $\mathcal{R}$ that we shall calculate in the results sections of this paper. In practice, we do not need to invert $\mathcal{G}_1^{22}$, nor do we need to write the equation for $\mathbf{F}^{\mathrm{c}}$ in block form. Instead, we compute $\mathcal{G}_1^{-1} \mathcal{P}$ by Gaussian elimination to find the force vectors that produce each standard rigid motion. The total forces and torques are then calculated to be $\mathcal{P}^{\mathrm{T}} \mathcal{G}_1^{-1} \mathcal{P} = \mathcal{R}$. The two equations for $\mathcal{R}$ can be seen to be equivalent by noting that the inverse of the expression in parentheses in Eq. (39) is equal to the upper-left block of $\mathcal{G}_1^{-1}$. This equivalence can be derived by block Gaussian elimination.

As we shall see, for some immersed boundary configurations, symmetry will reduce the dimension of the space of possible rigid motions V. In these cases, the above calculation does not change. Only the size of $\mathcal{R}$ will be affected. The same will be true if the immersed body has additional degrees of freedom, for instance in the case of multiple rigid bodies. Now, the dimension of V will be larger, but the calculation of constraint forces will be the same.

We have completely described a method of solution of the equations of the discrete immersed boundary method for a Stokes fluid coupled to an arbitrary configuration of immersed boundary points that move as a rigid body. We now apply this method to two types of configurations: a single immersed boundary point, meant to represent a sphere, and an array of points in a line, meant to represent a rigid cylinder. The results tell how well these Lagrangian discretizations truly represent spheres and cylinders.

3. Representing a sphere by a single immersed boundary point

We hypothesize that a single immersed boundary point in the discrete immersed boundary method is a good representation of a sphere of radius a, where a is to be determined. We would like that the resistance matrix of the immersed boundary point be close to the resistance matrix of a sphere of radius a, independent of the location of the immersed boundary point with respect to the grid. If the resistance matrices are close, then a force applied to an immersed boundary point will result in a velocity close to that of a sphere of radius a to which the same force is applied. We would also like the external velocity field generated by the immersed boundary point to be close to that generated by a sphere. We apply both these tests in this section.

Some interactions between a sphere and the fluid cannot be replicated by a single immersed boundary point. Immersed boundary points have no orientation, so it is impossible for a single point to rotate. Also, it is impossible to apply torque to a single point. The space V of rigid motions, introduced in Section 2.3 is three-dimensional and is the whole space of possible motions, so no constraint force is needed. Thus, the resistance matrix is 3×3: $\mathcal{R} = \mathcal{G}_1^{-1}$. In fact, because $\mathcal{G}(\mathbf{q}, \mathbf{q})$ is a diagonal matrix, $\mathcal{R}$ is also exactly diagonal.

We compare the results for an immersed boundary point to those for a sphere to which a force but no torque is applied. The resistance matrix of a sphere of radius a, ignoring torque and rotation, is a 3×3 matrix that is a multiple of the identity

$$\mathcal{R}_{\mathrm{sphere}} = 6\pi a \mathcal{I} \tag{41}$$

The drag on a sphere is isotropic and is proportional to the radius. Recall that we have set $\mu = 1$.

To test whether the resistance matrices of an immersed boundary point and a sphere are close, we perform the following procedure for each choice of approximate delta function and for each discretization method. We find the resistance matrices for a single immersed boundary point positioned at one of a large number (10,000) of randomly selected locations in a grid box. For each resistance matrix, we let the effective radius $a = \mathrm{tr}(\mathcal{R})/18\pi$, so that the resistance matrix has the same trace as that of a sphere of radius a. Averaging over all locations, we find the average effective radius, $\bar{a}$, for the particular choice of delta function and discretization method.

As a measure of error, we calculate $\epsilon = \|\mathcal{R}/6\pi\bar{a} - \mathcal{I}\|$ for each location, where the double bars indicate the matrix operator norm induced by the Euclidean vector norm. Precisely, ϵ is the maximum relative error in the drag force on an immersed boundary point in comparison to the drag on a sphere of radius $\bar{a}$ moving at the same velocity, where the maximum is over all orientations of this velocity. We let $\bar{\epsilon}$ be the maximum of ϵ over the 10,000 trials. Since ϵ is a continuous, periodic function of the position of the immersed boundary point, it has a finite maximum, and $\bar{\epsilon}$ will approach this maximum as the number of trials becomes very large.

Fig. 1 shows the results of the effective radii for different delta functions and discretization methods. The upper left plot shows a histogram of the effective radii obtained for δ_4^{IB} and the finite difference discretization. The mean of the distribution is $\bar{a} = 1.255$, so a single immersed boundary point interacts with the fluid like a sphere with radius 1.255 grid cells. The distribution does not have long tails and has a total width of only about 0.017, so for all of the 10,000 locations, a fell within 1% of $\bar{a}$.

The upper right corner shows a histogram of the effective radii obtained for δ_4^{IB} and the spectral discretization. The results are very similar to those for the finite difference method. The distribution has a similar shape, again without long tails, and is again very narrow. The lower left corner shows a histogram of the effective radii obtained for δ_4^{M} and the finite difference discretization. The distribution has a similar shape, but it is centered about a smaller value and is *much* wider than those for δ_4^{IB}. See Fig. 2 for a direct comparison. For some locations, a differed from $\bar{a}$ by almost 30%.

The lower right corner shows a summary of our findings for a variety of delta functions and for the finite difference discretization. Results for the spectral discretization (not shown) are very similar. Each point on this plot represents one choice of delta function. The horizontal coordinate shows $\bar{a}$, and the vertical coordinate shows $\bar{\epsilon}$. Each shape represents a different family of delta function. In each family, the delta functions with greater support (and thus higher interpolation order) have *smaller* $\bar{a}$ and smaller $\bar{\epsilon}$, so as the width of the support of δ increases, the points on the plot go down and to the left. The reason that $\bar{a}$ decreases for the delta
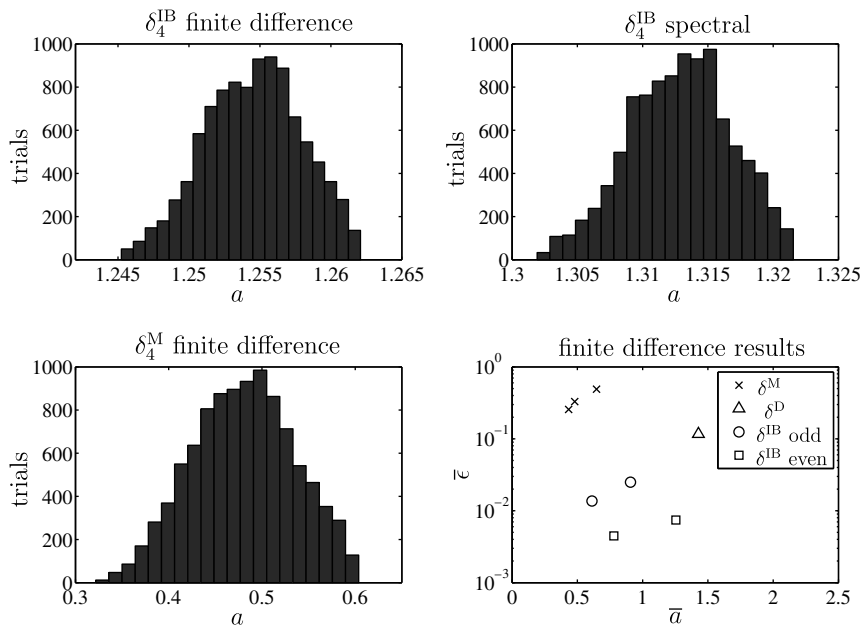
Fig. 1. Upper left: histogram of the effective radius a obtained using δ_4^{IB} and the finite difference discretization. Upper right: histogram of a obtained using δ_4^{IB} and the spectral discretization. Lower left: histogram of a obtained using δ_4^{M} and the finite difference discretization. Note the drastically different horizontal scale of this plot from those of the plots above (see also Fig. 2). Lower right: summary of the results obtained with various delta functions and the finite difference discretization. The maximum error $\bar{\epsilon}$ is plotted on a logarithmic scale against the mean effective radius $\bar{a}$. Each data point corresponds to one particular choice of delta function. Points with the same symbol correspond to delta functions in the same family. Within each family, delta functions with larger support have smaller $\bar{a}$ and smaller $\bar{\epsilon}$. For definitions of these functions, see Section 2.2 and the Appendix.
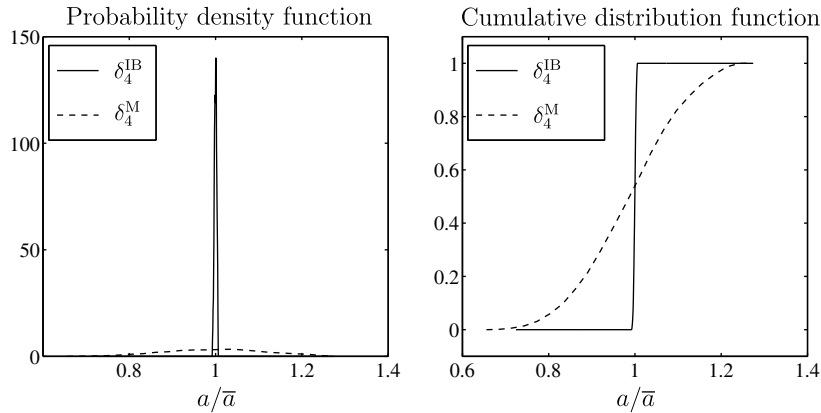
Fig. 2. Comparison of the effective radii obtained for δ_4^{IB} (solid line) and δ_4^{M} (dashed line). The plot on the left shows the probability density function of the scaled effective radius $a/\bar{a}$ for the two delta functions, inferred from the a obtained from 10,000 randomly selected locations of the immersed boundary point. The plot on the right shows the cumulative distribution function.

functions with greater support is that these have negative tails which serve to concentrate their masses closer to the origin. Functions in the family δ_d^{M} show large errors, at least 25%. Functions in the family δ_d^{IB} with d odd have errors around 2%. Functions in the family δ_d^{IB} with d even are best of all, with errors around 0.6%. The dilated function, δ_4^{D}, still shows a significant error. As a reference, the values of $\bar{a}$ and $\bar{\epsilon}$ for all the delta functions and for both discretization methods are tabulated at the end of this paper in Table 1.

In those cases in which one of the traditional immersed boundary delta functions, δ_d^{IB}, is used, an immersed boundary point does have a resistance matrix close to that of a sphere of a particular radius regardless of the location of the immersed boundary point with respect to the grid. This effective radius depends on which delta function (and somewhat upon which discretization method) is used. The figures suggest that the agreement improves as the support width of δ increases. Changing the discretization method does not appreciably change the results.

Having a delta function with a high interpolation order does not seem to be an advantage when it comes to representing a sphere by a single immersed boundary point. In fact, δ_4^{M}, with an interpolation order of 4 does not fare as well as δ_4^{D} with an interpolation order of 2. Much better, though, is δ_4^{IB} which has an interpolation order of 2 and also satisfies the sum of squares condition, Eq. (22). Generally, those delta functions that satisfy the sum of squares condition have very small $\bar{\epsilon}$ compared with those that do not.

While the role of the sum of squares and balanced conditions is unclear, these results are significant enough to suggest that the sum of squares condition is a good condition to impose on any delta function when representing a sphere by a single immersed boundary point. If the interaction of a single point with the fluid depends significantly on the location of the point with respect to the grid, it seems likely that the interaction of many points with the fluid will also depend significantly on their location with respect to the grid. Our results may imply that one should use a delta function that satisfies the sum of squares condition even when representing a more complicated solid boundary by many immersed boundary points. We test this hypothesis for the case of a rigid cylinder in the next section.

We now check whether the external velocity field created by an immersed boundary point is close to that created by a sphere of radius $\bar{a}$. The exact solution can be found for the external velocity field created when a force $\mathbf{F}$ is applied to a sphere of radius $\bar{a}$, centered at $\mathbf{x}_0$. The velocity is the sum of the Stokeslet, defined in Eq. (8) and a multiple of what is called the doublet, $\mathcal{D}_0$, applied to $\mathbf{F}$.

$$\mathcal{D}_0(\mathbf{x}) = \frac{1}{8\pi\mu} \frac{\mathcal{I} - 3\hat{\mathbf{x}}\hat{\mathbf{x}}^{\mathrm{T}}}{|\mathbf{x}|^3} \tag{42}$$

$$\mathbf{u}(\mathbf{x}) = \left(\mathcal{S}_0(\mathbf{x} - \mathbf{x}_0) + \frac{\bar{a}^2}{3} \mathcal{D}_0(\mathbf{x} - \mathbf{x}_0) \right) \mathbf{F} \tag{43}$$

For completeness, we show the scaling of the doublet with μ, even though μ is still set to one. A derivation of this solution can be found in Ref. [21], Section 4.9. Since the sphere is rigid, the interior velocity is everywhere $\mathbf{u} = \mathbf{F}/6\pi\mu a$.

To see whether the velocity created by an immersed boundary point is close to that created by a sphere, we choose one random location for the immersed boundary point in a grid box, $\mathbf{X}_0$, and a random force, $\mathbf{F}$ to be applied to the point. We then use Eqs. (18) and (24) to calculate $\mathbf{u}$ at grid points near $\mathbf{X}_0$. We compare these $\mathbf{u}$ with the exact solution for the velocity field of a sphere of radius $\bar{a}$ by calculating the relative error at every grid point and finding the L_2 average of this quantity over cubic shells of grid points around the immersed boundary point.

Fig. 3 shows the results of this procedure for δ_4^{IB} and the finite difference discretization. The plot on the left shows a two-dimensional slice of a vector field plot of the velocity, $\mathbf{u}$. For this plot, we chose $\mathbf{F} = \hat{x}$. The velocity has been translated by $-\mathbf{U}$ into the frame in which the immersed boundary point is stationary, so we can interpret the plot as showing the velocity field generated with the immersed boundary point held fixed and with a specified velocity equal to $-\mathbf{U}$ at infinity. The circle represents the effective surface of the immersed boundary point. It is the intersection of a sphere centered at $\mathbf{X}_0$ with radius $\bar{a}$ with the two-dimensional plane that is shown. Notice that the fluid velocity seems to approach zero on the sphere boundary as dictated by the no-slip condition. The velocity inside the boundary should be zero, and we observe small, but non-zero, velocities there.

The plot on the right shows the relative error in the velocity field as a function of the distance of the cubic shell from the immersed boundary point measured in the infinity norm. The relative error is small, even at small distances, and it declines as the distance from the point increases. For other delta functions and for the spectral discretization method, the results are similar. In particular, the errors are only slightly greater for delta functions in the family δ_d^{M}. This is likely because the velocity field at a distance of a few grid points from a sphere is not very sensitive to the radius of the sphere when the radius is on the order of a grid point. As seen earlier, however, for some delta functions the self-interaction of an immersed boundary point can vary wildly depending on the location of the point with respect to the grid.

When h is not equal to one, the resistance matrix of an immersed boundary point scales like $\mathcal{R}_h = h\mathcal{R}$. For general h an immersed boundary point will interact with the fluid like a sphere of radius $h\bar{a}$. If one wishes to represent a sphere of radius a_{S} by a single immersed boundary point, and one has chosen a delta function and a discretization method, then one should set $h = a_{\mathrm{S}}/\bar{a}$. We emphasize that our results recommend use of a
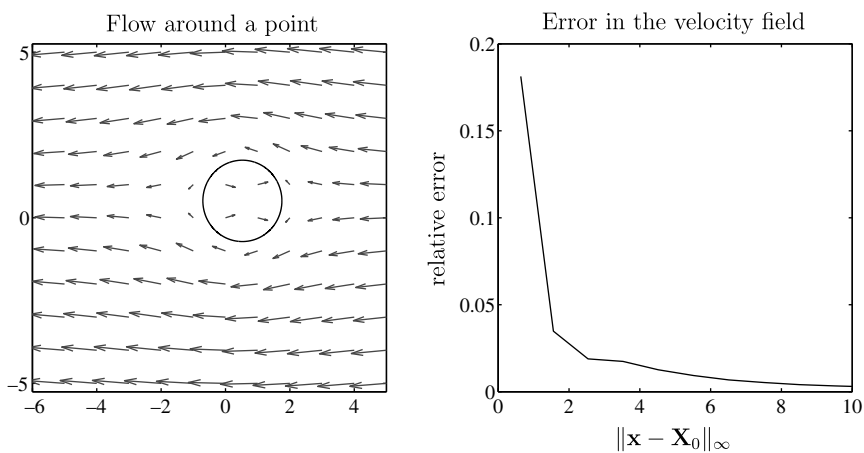
Fig. 3. Results obtained using δ_4^{IB} and the finite difference discretization. Left: two-dimensional slice of the three-dimensional vector field $\mathbf{u}$, for $\mathbf{F} = \hat{x}$. For clarity, the velocity field has been translated by $-\mathbf{U}$, so the immersed boundary point is at rest and there is a flow of $-\mathbf{U}$ at infinity. The circle shows the effective surface of the sphere represented by the immersed boundary point. This sphere has radius $\bar{a}$, which we found earlier by measuring the drag on immersed boundary points at many locations. Right: Relative error in $\mathbf{u}$ as a function of distance, averaged over cubic shells. Distance is measured in the infinity norm. The error decays rapidly with distance and is under 5% even at a distance of 2 grid cells.

delta function in the family δ_d^{IB} with d even or with d odd. It can be possible to represent spheres of several radii simultaneously by using a different delta function for each and by properly choosing h.

4. Representing a cylinder by a linear array of immersed boundary points

4.1. Computing the resistance matrix

We now consider the problem of representing a cylinder by a linear array of immersed boundary points that is constrained to move as a rigid body. We refer to such an array is a pseudo-cylinder. Our approach is similar to that for the sphere. We show that for certain choices of parameters the resistance matrix of a pseudo-cylinder is close to that of an actual rigid cylinder of a certain length and radius, independent of the position and orientation of the pseudo-cylinder with respect to the Eulerian grid. We then show that the external velocity field created by a pseudo-cylinder is also close to that created by an actual cylinder.

We have an additional parameter that we did not have to choose in the case of the sphere, namely the number of immersed boundary points in the array. We call this variable N, and in Section 4.2 we show that N can be chosen to minimize the position and orientation dependence of the resistance matrix of the pseudo-cylinder. We shall see that N can be too big as well as too small. Having chosen N, we compare the resistance matrix of a pseudo-cylinder with that of an actual cylinder in Section 4.3. We must pick the dimensions of the cylinder to which we want to compare. We call these the effective radius r and effective length $\tilde{L}$ of the pseudo-cylinder, and we show that these can be chosen in a natural way. Finally, in Section 4.4 we compare the generated velocity fields.

Although they need not necessarily be so, we consider only pseudo-cylinders made up of equally spaced immersed boundary points. We let L be the distance between the first and last points. Again, N is the number of immersed boundary points. The remaining parameters are the delta function, the discretization method, and the position and orientation of the pseudo-cylinder with respect to the grid.

An array of immersed boundary points in a straight line can translate in three directions and rotate in two, but cannot spin about its axis; force can be applied in three directions and torque in two. So, the space V is five-dimensional and the resistance matrix $\mathcal{R}$ is five by five. A slight modification is needed to the procedure described in Section 2.3. We use a basis for V different from the translations and rotations in the coordinate directions. We identify the unit tangent vector to the centerline of the pseudo-cylinder, $\mathbf{t}$, choose an arbitrary unit normal vector $\mathbf{n}_1$, and let $\mathbf{n}_2 = \mathbf{t} \times \mathbf{n}_1$. We let $\mathbf{X}_0$ be the mean position of the immersed boundary points. As a basis for V we pick the elementary translations, $\mathbf{U} = \mathbf{t}$, $\mathbf{n}_1$, and $\mathbf{n}_2$, and the elementary rotations, $\mathbf{U}(\mathbf{q}) = \mathbf{n}_1 \times (\mathbf{X}(\mathbf{q}) - \mathbf{X}_0)$ and $\mathbf{n}_2 \times (\mathbf{X}(\mathbf{q}) - \mathbf{X}_0)$. We then calculate $\mathcal{R}$ as described in Section 2.3.

By the symmetries of a cylinder, we expect $\mathcal{R}$ to be close to diagonal in this basis. Forces or torques in one of these directions should not cause motion in another. The diagonal elements are the translational and rotational drags of the array. We expect the drag in the $\mathbf{n}_1$ and $\mathbf{n}_2$ directions to be approximately equal. We also expect the rotational drag in the $\mathbf{n}_1$ and $\mathbf{n}_2$ directions to be approximately equal. For definiteness, when presenting results we refer to the drag in the $\mathbf{n}_1$ direction as the normal drag, and we refer to the rotational drag in the $\mathbf{n}_1$ direction as the rotational drag.

For a given choice of delta function, discretization method, L, and N, we calculate the resistance matrix of 100 pseudo-cylinders with randomly selected positions and orientations with respect to the grid. We find the mean resistance matrix, $\mathcal{R}_{mean}$, and also the five by five matrices $\mathcal{R}_{min}$ and $\mathcal{R}_{max}$ whose entries are the minimum and maximum values of the entries of $\mathcal{R}$ over the 100 trials. The resistance matrix is a continuous, periodic function of the position and orientation of the pseudo-cylinder, so its entries have finite maximums and minimums. For a large number of trials, the entries $\mathcal{R}_{min}$ and $\mathcal{R}_{max}$ will approach these extremal values.

To quantify the difference between $\mathcal{R}$ for a trial and $\mathcal{R}_{mean}$, we should take into account that the eigenvalues of $\mathcal{R}_{mean}$ vary greatly in magnitude. To this end, we define a measure of position and orientation dependence, σ, as follows:

$$\sigma = \|\mathcal{R}_{mean}^{-1/2} \mathcal{R} \mathcal{R}_{mean}^{-1/2} - \mathcal{I}\| \tag{44}$$

The double bars again indicate the matrix operator norm induced by the Euclidean vector norm. This definition gives equal weight to each eigendirection of $\mathcal{R}_{mean}$. Precisely, σ is the maximum relative deviation in the

drag forces and torques on a cylinder moving with some specified translational and rotational velocities, provided we use the norm induced by the symmetric matrix $\mathcal{R}_{\mathrm{mean}}^{-1}$ to measure the sizes of vectors: $\|\mathcal{F}\|^2 = \mathcal{F}^{\mathrm{T}} \mathcal{R}_{\mathrm{mean}}^{-1} \mathcal{F}$. We let $\bar{\sigma}$ be the maximum of σ over the 100 trials.

4.2. Choosing the number of immersed boundary points

We determine the appropriate number of points, N, to use for each L. For a good choice of N, we would like the resistance matrix to be close to diagonal and to be nearly independent of the position and orientation of the pseudo-cylinder with respect to the grid. We would also like our choice of N to be robust, meaning we do not want our resistance matrices to depend sensitively on the exact choice of N. Further, we would like N to be proportional to L so that there is an appropriate range of densities of immersed boundary points. We define the immersed boundary point density to be $\rho = (N-1)/L$. A robust choice of N that results in a consistent, accurate resistance matrix suggests that even a non-rigid slender body may be accurately represented by an array of immersed boundary points.

We first investigate the limit as N approaches infinity. Calculations using large N are expensive, so we restrict our investigation to the special case $L = 20$, to the finite difference discretization method, and to δ_4^{IB}, δ_4^{M}, and δ_6^{IB}. We let N vary from 5 to 400 in increments of 5. At very large densities, we occasionally find that $\mathcal{R}$ has extremely large values, probably because the matrix $\mathcal{G}_1$ is nearly singular in this case, and so the condition number for the computation of $\mathcal{R}$ can be large. To exclude these anomalies, we let $\mathcal{R}_{\mathrm{mean}}$ be the trimmed mean, excluding the largest and smallest 5% of values in each component. Similarly, $\mathcal{R}_{\mathrm{min}}$ and $\mathcal{R}_{\mathrm{max}}$ are the minimum and maximum values of each component excluding the largest and smallest 5%, and $\bar{\sigma}$ excludes that largest 10% of trials. These changes only apply to the results in this investigation of large N.

Results for high densities of immersed boundary points are seen in Fig. 4. The solid lines show the trimmed mean tangential drag and normal drag as a function of the density ρ. The dashed lines on either side of the solid lines show the trimmed maximum and minimum drags. For all choices of delta function, the drags seem to converge to a limit as ρ becomes very large, but with significant position and orientation dependence. Our quantitative measure of orientation dependence, $\bar{\sigma}$, is very large for large ρ: around 25% for δ_4^{IB} and δ_4^{M} and 45% for δ_6^{IB}.

We can do better by focussing more closely on the regime of small ρ. We now use all choices of delta function and both discretization methods. We let L vary from 2 to 52 in increments of 2, and we let N vary over all integers between 2 and $3L + 1$ so that ρ is between 0 and 3.

Fig. 5 shows results for δ_4^{IB} and the finite difference discretization. Results are shown for several values of L, ranging from 10 to 50 in increments of 10, with darker lines indicating smaller values. The plots show drag in the tangential, normal, and rotational directions, as well as the off-diagonal component of $\mathcal{R}$ that couples together the two normal directions. This component ought to be close to zero. Results for the other off-diagonal components are similar.

This figure shows that, to a remarkable degree, the qualitative behavior of $\mathcal{R}$ as a function of the number of immersed boundary points depends only on the density of immersed boundary points, independent of the cylinder length. This is a very fortunate result, because if we are interested in using an array of immersed boundary points to represent a cylinder, we need only determine the best value of ρ, not the best value of N for every L. Moreover, we can be more confident in representing a non-rigid slender body by an array of immersed boundary points, because there seems to be a preferred range of local densities, a fact that will not change if the body has small curvature, i.e. curvature with radius that is large in comparison to the grid spacing.

At small ρ, the drags increase sharply as density increases, indicating that the immersed boundary points are still allowing fluid to pass between them. At densities between 0.4 and 1.0, the drags are all very flat as functions of density, the maximum and minimum drags are very close to the mean drag, and coupling between the two normal directions is insignificant. At higher densities, the mean drag begins to increase as a function of ρ, the maximum and minimum drags diverge from the mean, and the maximum and minimum coupling between the two normal directions ceases to be negligible compared to the normal drag. We know from Fig. 4 that at very large ρ the mean, maximum, and minimum drags converge eventually, but to values where there is significant orientation and position dependence.
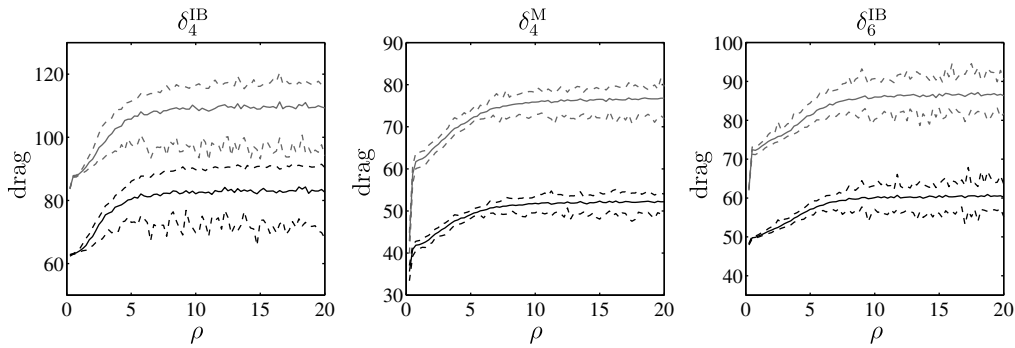
Fig. 4. Results for high densities of immersed boundary points. The solid lines show mean drag in the normal (shown by lighter lines) and tangential (shown by darker lines) directions as a function of immersed boundary point density ρ. $L = 20$, and we use the finite difference discretization. Dashed lines show the maximum and minimum drags in these directions. Left: results for δ_4^{IB}. Center: results for δ_4^M. Right: results for δ_6^{IB}. In all cases, as ρ becomes very large, the mean, maximum, and minimum drags seem to converge to a finite limit. At this limit, the drags depend significantly on the position and orientation of the pseudo-cylinder.
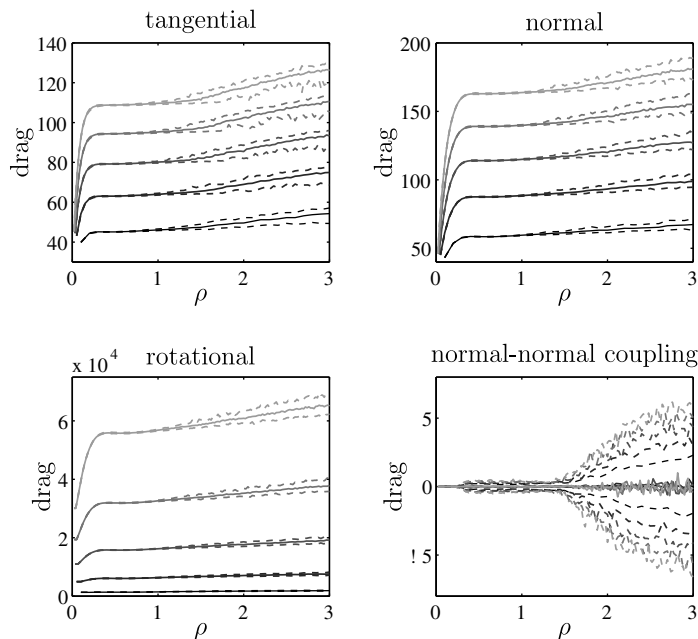
Fig. 5. Results for low densities of immersed boundary points. Plots showing drags for δ_4^{IB} and the finite difference discretization as a function of immersed boundary point density. Solid lines show mean drags. Dashed lines show maximum and minimum drags. Results are shown for $L = 10, 20, 30, 40$, and 50 with shorter lengths represented by darker lines. Upper left: tangential drag. Upper right: normal drag. Lower left: rotational drag. Lower right: off-diagonal element of $\mathcal{R}$ showing drag in one normal direction as a result of velocity in the orthogonal normal direction. We note that the qualitative behavior of the drags seems to depend only on ρ, and not on L and N independently. Moreover, there is a range of densities, $0.4 < \rho < 1.0$, where the drags are approximately constant, independent of position and orientation, and where there is little off-diagonal coupling.

We see the same qualitative behavior with different delta functions and discretization methods, as seen in Fig. 6. The upper left plot in this figure, which is for δ_4^{IB} and the spectral discretization, is nearly identical to the upper right plot in Fig. 5. As when representing a sphere, the choice of discretization method made little difference in the results for any delta function.

The plots for δ_4^D, δ_6^{IB}, and δ_5^{IB} are qualitatively similar to that for δ_4^{IB}. There is a distinct range of ρ where the normal drag is approximately position and orientation independent and also independent of N. This range is much smaller for δ_4^D than for the immersed boundary method delta functions. Surprisingly, the orientation and

position dependence in this range is largest for δ_6^{IB}. On the other hand, the divergence of the maximum and minimum drags from the mean for large ρ and the slope of the mean drag at large ρ are smaller. If we compare back to the rightmost plot in Fig. 4, we see that the divergence eventually becomes large for very large ρ.

Less similar are the plots for δ_4^{M} and δ_6^{M}. While the drag increases as a function of ρ at large ρ, it does not seem as though the maximum and minimum drags diverge from the mean. We again refer back to Fig. 4 to see that this does occur at very large ρ. For these two delta functions there is significant position and orientation dependence for all choices of ρ, and the range where the mean drag is independent of ρ is small.

The quantitative position and orientation dependence of the resistance matrices as a function of density for the various delta functions can be seen more clearly in Fig. 7. Here, our measure of position and orientation dependence, $\bar{\sigma}$, is plotted against ρ for various delta functions, for the finite difference discretization, and for the case $L = 30$. Results for the spectral discretization and for different L are similar. Delta functions in the family δ_d^{IB} have $\bar{\sigma}$ less than 5% provided the density is less than about 1. Delta functions in the family δ_d^{M} have $\bar{\sigma}$ greater than 10% for all densities, but seem to have a minimum position and orientation dependence at a density of around 1. Finally, the function δ_4^{D} requires a density somewhat less than 1 to achieve a small $\bar{\sigma}$.

For every delta function there is a finite range of densities, which we call the preferred range, in which the position and orientation dependence of the resistance matrix is minimal, in which the resistance matrix does not depend sensitively on the exact choice of density, and in which the resistance matrix is nearly diagonal. This density interval tends to be near 1. Its exact location and size depends on the delta function and, less so, on the discretization method used.

To proceed, we choose a specific preferred density for each delta function and discretization method. The exact choice is not important, as long as it falls within the preferred range. Two possible choices, which can serve as rules of thumb, are densities of 1.0 and of $1/\bar{a}$, where $\bar{a}$ is the effective radius of an immersed boundary point as explained in the Section 3 on representing a sphere. In the first case, immersed boundary points are placed one grid cell apart. In the second case, they are placed one effective radius apart. The traditional rule of
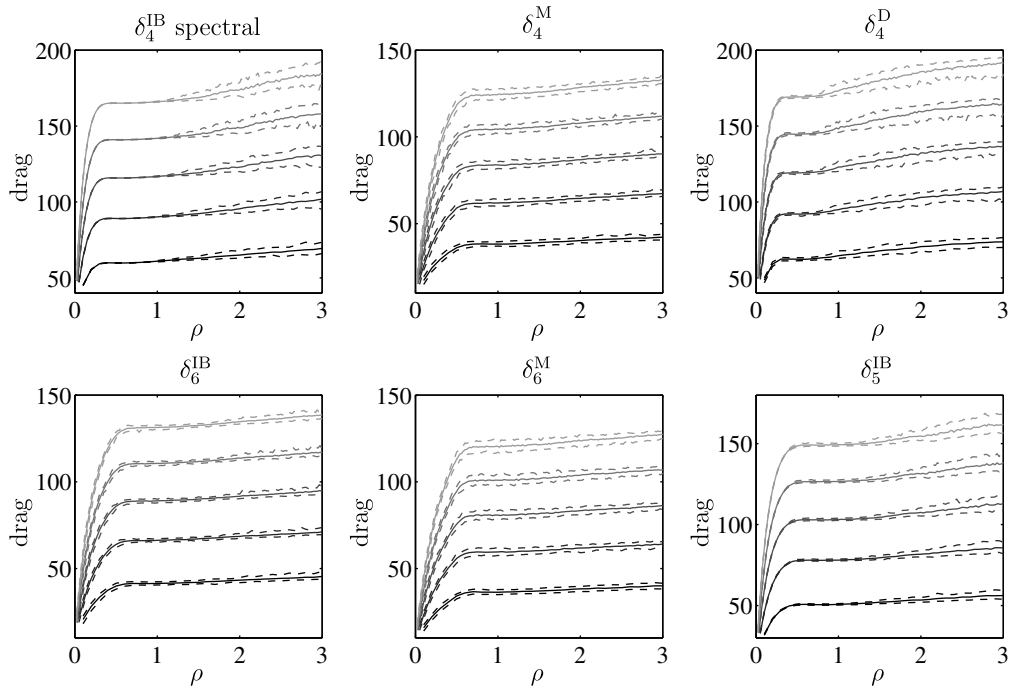
Fig. 6. Plots showing normal drags for different delta functions and discretization methods as a function of immersed boundary point density. Solid lines show mean drags. Dashed lines show maximum and minimum drags. Results are shown for $L = 10$, 20, 30, 40, and 50 with shorter lengths represented by darker lines. Upper left: δ_4^{IB} and the spectral discretization. The remaining plots use the finite difference discretization. Upper middle: δ_4^{M}. Upper right: δ_4^{D}. Lower left: δ_6^{IB}. Lower middle: δ_6^{M}. Lower right: δ_5^{IB}. The results are similar to those for δ_4^{IB} with the finite difference discretization shown in Fig. 5.

thumb used in immersed boundary method computations is that points be spaced approximately half a grid cell apart, corresponding to a density of 2.0. This density is recommended to avoid leaks in computations in which regions of fluid are bounded by thin surfaces made up of immersed boundary points. Our purpose here is quite different, and we see in Figs. 6 and 7 that such a large density would be inappropriate for representing a cylinder by an array of points.

In our results presented below, we use a density of 1.0 for all delta functions except δ_4^{IB} and δ_4^{D}, for which we use $1/\bar{a}$. These choices nearly minimize $\bar{\sigma}$. For a particular value of L, we choose the integer number of points, N, that best approximates the desired density.

Having chosen N, we examine the position and orientation dependence of the resistance matrix as a function of L. Fig. 8 shows $\bar{\sigma}$ for various delta functions and discretization methods. Solid lines show results for the finite difference discretization. Dashed lines show results for the spectral discretization. For most delta functions, the spectral discretization results in somewhat smaller position and orientation dependence than the finite difference discretization.

The delta function δ_4^{IB} has the smallest $\bar{\sigma}$, below 1% for all L greater than 10. We find larger $\bar{\sigma}$ for δ_6^{IB}, though still below 5% for almost all L. When L takes its smallest values, only a few immersed boundary points are used to represent the cylinder (approximately $L + 1$). Under these circumstances, it is surprising that the representation works as well as it does. We find much larger $\bar{\sigma}$ for δ_4^{M} and δ_6^{M}: over 5% for the entire range of L when using the finite difference discretization. When L is smaller than 10, $\bar{\sigma}$ is greater than 15%. In all cases, this is a vast improvement over the values of $\bar{\sigma}$ we obtained for very large values of ρ which were at least 25%, even when trimmed to exclude the worst 10% of trials.

4.3. Comparing to the results for a cylinder

We now investigate whether the mean resistance matrix of a pseudo-cylinder with the preferred choice of N is close to that of a rigid cylinder of some radius r and of length $\widetilde{L}$. Unfortunately, no exact solution to the external velocity field of a translating or rotating cylinder has been found, so no exact value for the resistance matrix is available. Instead, we use an approximation from slender-body theory

$$\mathcal{R}_{11} = \frac{2\pi\widetilde{L}}{\log 2\widetilde{L}/r - \frac{3}{2} - \left(1 - \frac{\pi^2}{12}\right)(\log \widetilde{L}/r)^{-1}} + \mathrm{O}[\widetilde{L}(\log \widetilde{L}/r)^{-4}]$$

$$\mathcal{R}_{22} = \mathcal{R}_{33} = \frac{4\pi\widetilde{L}}{\log 2\widetilde{L}/r - \frac{1}{2} - \left(1 - \frac{\pi^2}{12}\right)(\log \widetilde{L}/r)^{-1}} + \mathrm{O}[\widetilde{L}(\log \widetilde{L}/r)^{-4}] \qquad (45)$$

$$\mathcal{R}_{44} = \mathcal{R}_{55} = \frac{\pi\widetilde{L}^3/3}{\log 2\widetilde{L}/r - \frac{11}{6} - \left(\frac{10}{9} - \frac{\pi^2}{12}\right)(\log \widetilde{L}/r)^{-1}} + \mathrm{O}[\widetilde{L}^3(\log \widetilde{L}/r)^{-4}]$$
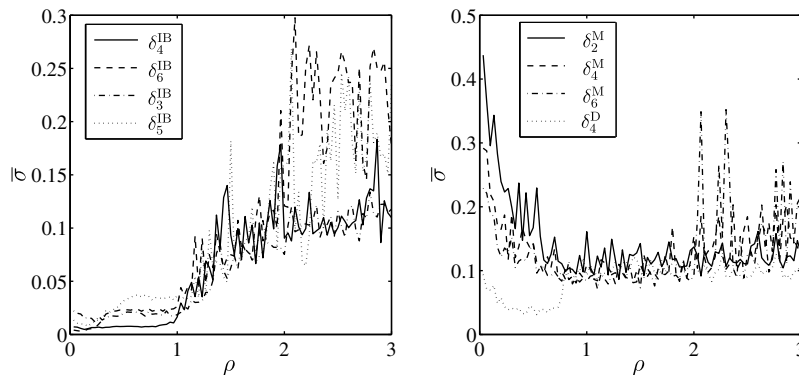
Fig. 7. Position and orientation dependence of the pseudo-cylinder resistance matrices as a function of the density ρ. The quantity $\bar{\sigma}$ is a measure of maximum relative deviation (see Eq. (44)). For delta functions in the families δ_d^{IB} with d odd or even, $\bar{\sigma}$ is small when ρ is less than 1. Delta functions in the family δ_d^{M} never have $\bar{\sigma}$ below 10%, though $\bar{\sigma}$ still has a local minimum at a density of about 1.
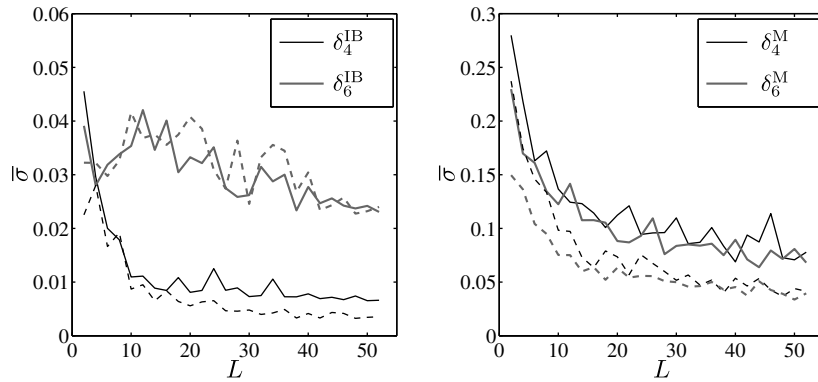
Fig. 8. Position and orientation dependence of the pseudo-cylinder resistance matrices as a function of the length L at the preferred immersed boundary point density. Solid lines show $\bar{\sigma}$ for the finite difference discretization. Dashed lines show $\bar{\sigma}$ for the spectral discretization. In the plot on the left, darker lines show results for δ_4^{IB}, and lighter lines show results for δ_6^{IB}. In the plot on the right, darker lines show results for δ_4^{M}, and lighter lines show results for δ_6^{M}. Note the difference in vertical scale between the plots on the left and those on the right. The delta functions traditionally used in the immersed boundary method (left) result in deviations below 5% for the entire range of L. Deviations obtained with the delta functions in the family δ_d^{M} are much larger.

The off-diagonal elements of $\mathcal{R}$ are all equal to zero. The expressions for the tangential and normal drag are derived in Keller and Rubinow [22]. The expression for rotational drag can be derived by the method presented in their paper. The derivation of the above equations uses a fixed point iteration to solve approximately the slender-body theory integral equation. For a cylinder, the exact solution of this integral equation may be unphysical because of endpoint problems [23,24]. Still, Eq. (45) should be a valid approximation, and it is in good agreement with numerical solutions of the Stokes equations as well as experimental results [25]. This approximation is only valid for small $r/\widetilde{L}$.

We now consider how to choose the effective radius and effective length of the pseudo-cylinder in our computations for comparison with Eq. (45). For the effective length, we would like to find a correction, $\delta L = \widetilde{L} - L$, that is valid for all pseudo-cylinder lengths, L. The obvious approach would be to fit r and δL to the pseudo-cylinder data. However, the sensitivity of the slender-body theory resistance matrix to changes in these quantities is proportional to, respectively, $1/(r \log \widetilde{L})$ and $1/\widetilde{L}$, which become small as $\widetilde{L}$ becomes large. Therefore, the fit of r and δL becomes increasingly sensitive to the pseudo-cylinder resistance matrices as $\widetilde{L}$ becomes large. For this reason, we do not fit r and δL. Instead, we use heuristic arguments to arrive at guesses for their values. These guess are then justified by comparing the mean drags of the pseudo-cylinders with Eq. (45).

The first heuristic argument is geometric. Suppose that spheres of radius a are placed in a linear array such that each just touches its neighbor. Suppose now that a cylinder of radius r is of the same length as this array of spheres and also occupies the same volume. The volume of each segment of cylinder of length $2a$ must be the same as the volume of each sphere. The radius of the cylinder must then be $\sqrt{2/3}a$. If L is the distance between the centers of the first and last sphere, then the cylinder will have total length $L + 2a$. We know from the previous section that an immersed boundary point acts approximately like a sphere of radius $\bar{a}$. This suggests that we use $\sqrt{2/3}\bar{a}$ as our guess for the effective radius r and $2\bar{a}$ as our guess for the effective length correction δL. This geometric analogy is not perfect, for we have shown that it often optimal to place the immersed boundary points closer together than $2\bar{a}$.

A second heuristic argument confirms the above guess for r. Consider a slender body in Stokes flow whose centerline position is given by $\mathbf{X}(s)$, where s, an arclength parameter, varies from 0 to $\widetilde{L}$. The body is locally a cylinder, and its local radius is $r(s)$. The one-dimensional force density applied by the body to the fluid is $\mathbf{F}(s)$. Then, the velocity field can be approximated by the following integral [22–24]

$$\mathbf{u}(\mathbf{x}) = \int_0^{\widetilde{L}} \left(\mathcal{S}_0(\mathbf{x} - \mathbf{X}(s)) + \frac{r(s)^2}{2} \mathcal{D}_0(\mathbf{x} - \mathbf{X}(s)) \right) \mathbf{F}(s)\, \mathrm{d}s \tag{46}$$

The Stokeslet, $\mathcal{S}_0$, is defined in Eq. (8). The doublet, $\mathcal{D}_0$, is defined in Eq. (42). The far-field velocity is the sum of the local contributions of the forces. Each element of force creates a velocity equal to the force multiplied by the Stokeslet plus $r^2/2$ times a doublet, where r is the local radius. Recall from Eq. (43) that the velocity field created by a sphere of radius a is the applied force multiplied by the sum of a Stokeslet and $a^2/3$ times a doublet. So, the velocity field created by a slender body is asymptotically the same as the sum over s of the velocity fields created by spheres placed along the centerline of the body at $\mathbf{X}(s)$, with radii $a(s) = \sqrt{3/2}r(s)$, to which the force density $\mathbf{F}(s)$ is applied. Our pseudo-cylinder is composed of immersed boundary points which act like spheres of radius $\bar{a}$. Therefore, the velocity field it creates will be similar to that of a cylinder of radius $r = \sqrt{2/3}\bar{a}$.

In summary, for the purposes of comparing the pseudo-cylinder resistance matrices with Eq. (45), we use $\sqrt{2/3}\bar{a}$ for the effective radius, r, and $2\bar{a}$ for the effective length correction, δL, so that $\widetilde{L} = L + 2\bar{a}$. These guesses are intuitively reasonable: the effective length of a pseudo-cylinder is slightly larger than the distance between the first and last immersed boundary points by an amount on the order of the effective point radius, and the effective radius of a pseudo-cylinder is also on the order of the effective point radius.

Fig. 9 shows the mean drags in the tangential, normal, and rotational directions for pseudo-cylinders as functions of length compared with the formulas derived from slender-body theory given in Eq. (45). The slender-body theory results are for for cylinders with lengths $\widetilde{L} = L + 2\bar{a}$ and radii $r = \sqrt{2/3}\bar{a}$. Note, in particular, that the results shown in Fig. 9 were obtained without any additional adjustment of parameters. Agreement is nearly perfect, except at very small values of L, for which slender-body theory does not give an accurate approximation. The differences at larger values of L are on the order of the error term term for the slender-body theory approximation. Results for other delta functions and for the spectral discretization (not shown) are similar to those in Fig. 9.

To quantify the differences between $\mathcal{R}_{\text{mean}}$ and the resistance matrices implied by the slender-body theory formulas, $\mathcal{R}_{\text{sb}}$, we define $\epsilon = \|\mathcal{R}_{\text{sb}}^{-1/2}\mathcal{R}_{\text{mean}}\mathcal{R}_{\text{sb}}^{-1/2} - \mathcal{I}\|$. Fig. 10 shows ϵ as a function of L for various delta functions and the finite difference discretization. The relative differences are under 5% except when L is small and slender-body theory is not valid. The differences are somewhat, but not substantially smaller for the delta functions traditionally used in the immersed boundary method as opposed to those in the family δ_d^{M}.

The behavior of ϵ as $L \to \infty$ cannot be seen clearly in Fig. 10. We conjecture, however, that $\epsilon \to 0$ as $L \to \infty$. If, in fact, ϵ does converge to zero, then the pseudo-cylinder will, asymptotically, have the same mean resistance matrix as a cylinder. This is because the slender-body theory resistance matrix is asymptotically that of a cylinder. If the position and orientation dependence, $\bar{\sigma}$, also converges to zero as Fig. 8 seems to indicate, then the pseudo-cylinder will asymptotically have the same resistance matrix as a cylinder, regardless of its position and orientation relative to the grid. As in slender-body theory, the asymptotic convergence is in the limit of the aspect ratio $r/\widetilde{L}$ decreasing to zero. In particular, this asymptotic convergence will occur for a pseudo-cylinder of fixed length in the limit as the grid spacing decreases to zero. Unless we have chosen the effective radius r exactly correctly, the best convergence rate that we can obtain for the relative error in the resistance matrix is $O([\log(L/r)]^{-1})$. This rate seems consistent with the results in Fig. 10. To confirm convergence, we need to investigate larger values of L.

We conclude that, regardless of the delta function or discretization method, a linear array of immersed boundary points that are constrained to move as a rigid body have a mean resistance matrix very similar to that of a cylinder of length $\widetilde{L} = L + 2\bar{a}$ and radius $r = \sqrt{2/3}\bar{a}$. This conclusion depends on our having chosen the correct density of immersed boundary points. We chose either 1.0 or $1.0/\bar{a}$, but any value in the preferred range would suffice. If we, however, had chosen a larger density, we would have gotten mean drags that were too large, as can be seen in Figs. 4–6.

Even though the mean resistance matrix of a pseudo-cylinder is close to that of an actual cylinder for all delta functions and discretization methods, the position and orientation dependence of the resistance matrix is larger for those delta functions in the family δ^{M} and also for δ_4^{D}. If those delta functions traditionally used in the immersed boundary method, δ^{IB}, are employed, the resistance matrix accurately matches that of a cylinder and also is essentially independent of the position and orientation of the pseudo-cylinder, as desired.
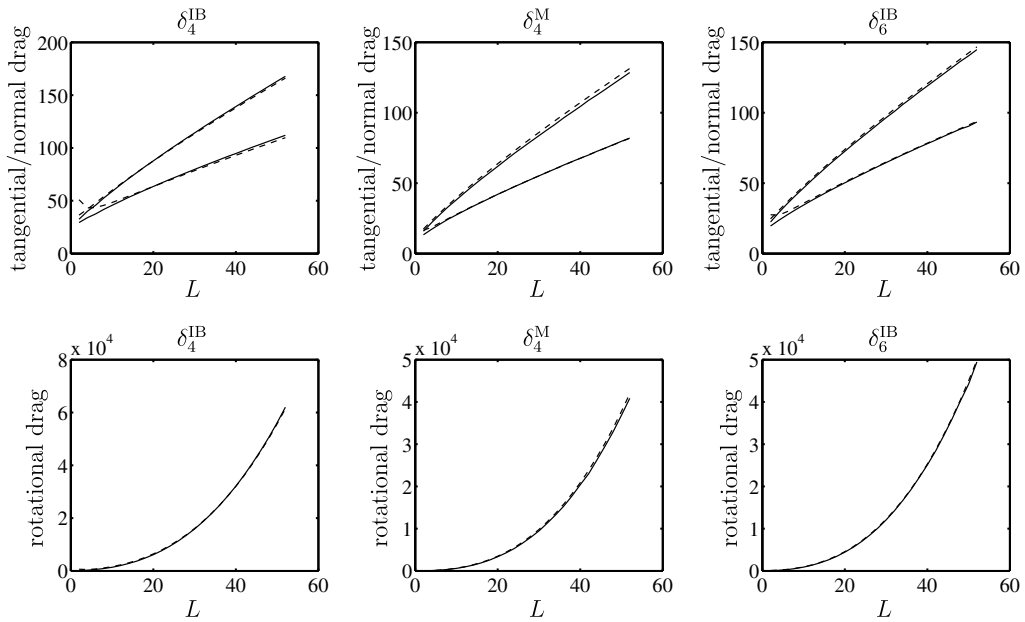
Fig. 9. Mean drag on a pseudo-cylinder as a function of length compared to formulas from slender-body theory (Eq. (45)) for various delta functions and the finite difference discretization. The pseudo-cylinder results are shown by solid lines. The slender-body theory formulas are shown by dashed lines. The top row of plots shows drag in the tangential and normal directions. In all cases, normal drag is larger than tangential drag. (It is customary to say that the normal drag is twice the tangential drag, but this, in fact, is only true in the limit $\widetilde{L} \to \infty$, and that limit is approached only slowly. See Eq. (45).) The bottom row shows drag in the rotational direction. Agreement is very good except at very small lengths, for which the slender-body theory formulas are not accurate.
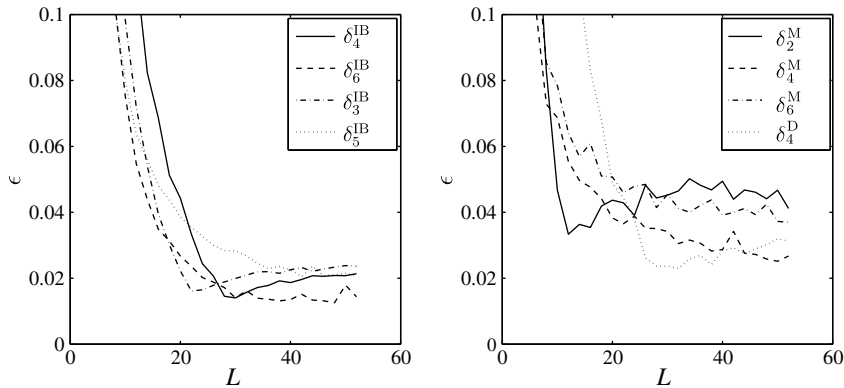
Fig. 10. Norm of the difference between the mean resistance matrix of a pseudo-cylinder and the resistance matrix obtained from the slender-body theory formulas as a function of length for various delta functions. The difference is small for all delta functions except at small lengths where slender-body theory is invalid.

4.4. Comparing velocity fields

As a final test, we examine the external velocity fields created by a pseudo-cylinder and compare with slender-body theory. We specify the velocities of the immersed boundary points, $\mathbf{U}(\mathbf{q})$, so that $\mathbf{U}$ is a standard basis element in the space of rigid body motions, V. The unique force that will produce this motion, by Eq. (30), is $\mathbf{F} = \mathcal{G}_1^{-1}\mathbf{U}$. The decomposition of $\mathbf{F}(\mathbf{q})$ into applied force and constraint force is arbitrary, provided that there is no net force or torque applied by the constraint force. Once we have found $\mathbf{F}(\mathbf{q})$, we may find the velocity $\mathbf{u}$ at any grid point using Eqs. (18) and (24).

We compute **u** at every grid point in a large rectangular box surrounding a pseudo-cylinder. We perform these computations for the particular choice of $L = 30$ and, for ease of visualization, we use a pseudo-cylinder whose tangent and normal vectors are aligned with the grid. The mean position, $\mathbf{X}_0$, is chosen randomly. We report results only for the finite difference discretization and for the delta function δ_4^{IB}. For this delta function and discretization method, we use 25 immersed boundary points, which best approximates a density of $1/\bar{a}$. Results with other delta functions and discretization methods are similar.

There is no known exact solution for the velocity field created by a cylinder undergoing rigid motion, so we compare the velocity field of a pseudo-cylinder with the approximation from slender-body theory. The slender body has the same position and orientation as the pseudo-cylinder, but extends past the endpoints of the pseudo-cylinder by a distance $\bar{a}$ on each side. We specify the velocity of the cylinder to be a rigid body motion. The force density $\mathbf{F}(s)$ is determined by approximately solving an integral equation using a fixed point iterative method as described in Ref. [22]. We then use quadrature to compute the slender-body velocities, according to Eq. (46), at the same set of grid points for which velocities are computed for the pseudo-cylinder. We denote these velocities by $\mathbf{u}^{SB}$, which we compare to the pseudo-cylinder velocities **u**. Eq. (46) is only valid in the exterior of the cylinder, and we set $\mathbf{u}^{SB}$ to be the exact rigid body motion velocity inside the cylinder.

Figs. 11–13 show two-dimensional slices of **u** (top) and $\mathbf{u}^{SB}$ (bottom) for cylinders moving in the the tangential, normal, and rotational directions. In each case, the velocities have been modified by subtracting a solution of the Stokes equations so that we depict the velocity field created by a fixed rigid cylinder in an incident flow from infinity. The rectangle in these plots shows the intersection of the two-dimensional plane depicted with the surface of a cylinder of radius r and length $\widetilde{L}$. The rectangle is the effective surface of the pseudo-cylinder in this plane.

In each figure, the two velocity fields are very similar. Qualitatively, **u** appears to be close to zero on the effective surface of the pseudo-cylinder, as dictated by the no-slip condition, and to be nearly zero inside the surface. Larger, non-zero velocities appear near the endpoints of the cylinder. Pictorially, the effective length of the psuedo-cylinder $\widetilde{L}$, which is the length of the red box, seems to be a good choice, as does the effective radius r. The slender-body theory approximation, $\mathbf{u}^{SB}$ is identically zero inside the cylinder's surface, but appears to take several slightly unusual values near the endpoints of the cylinder. Indeed, slender-body theory is not valid near these points [23].

To compare **u** and $\mathbf{u}^{SB}$ quantitatively, we want to exclude the difference that comes from the different total forces or torques being applied to the fluid in each case, which come about because of the small differences in drags described above. To exclude this source of difference between **u** and $\mathbf{u}^{SB}$, we normalize each by the appropriate drag (tangential for tangential motion, etc.). For translational motion, we are comparing velocity fields that arise from the same total force applied to the fluid, and for rotational motion, we are comparing velocity fields that arise from the same total torque applied to the fluid. We calculate the relative difference $|\mathbf{u} - \mathbf{u}^{SB}|/|\mathbf{u}^{SB}|$ and calculate the L_2 average of this quantity on rectangular shells of grid points surrounding the cylinder. On each shell, the infimum of $\|\mathbf{x} - \mathbf{X}(s)\|_\infty$ over s is approximately constant, and we calculate the L_2 average of this quantity. Note that this is the distance of the shell from the axis of the cylinder, not from the cylinder's surface.

Fig. 14 shows the average relative difference in **u** and $\mathbf{u}^{SB}$ over a shell as a function of the average infinity norm distance of the shell from the axis of the cylinder. Note that this plot shows the difference between results obtained by two approximate methods. No exact solution is available for comparison. The solid line is for translational motion tangential to the cylinder's axis, the dashed line is for translational motion normal to the cylinder's axis, and the dotted line is for rotational motion. In the translational cases, the relative difference in the velocity fields is below 6% even up to and inside the surface of the cylinder. This difference decays rapidly as the rectangular shell of grid points gets farther from the cylinder. The relative difference in the rotational case is larger, but is still below 11% everywhere in the exterior of the surface of the cylinder. This difference also decays rapidly, becoming 2% at a distance of 25 grid cells.

We conclude that the velocity fields created by a pseudo-cylinder are close to the slender-body theory approximations for the velocity fields, which are presumably close to the velocity fields created by an actual cylinder. As a result, the interactions of a pseudo-cylinder with external bodies in the fluid will be similar to the interactions of a cylinder with those bodies. We saw above that the resistance matrix which describes the self-
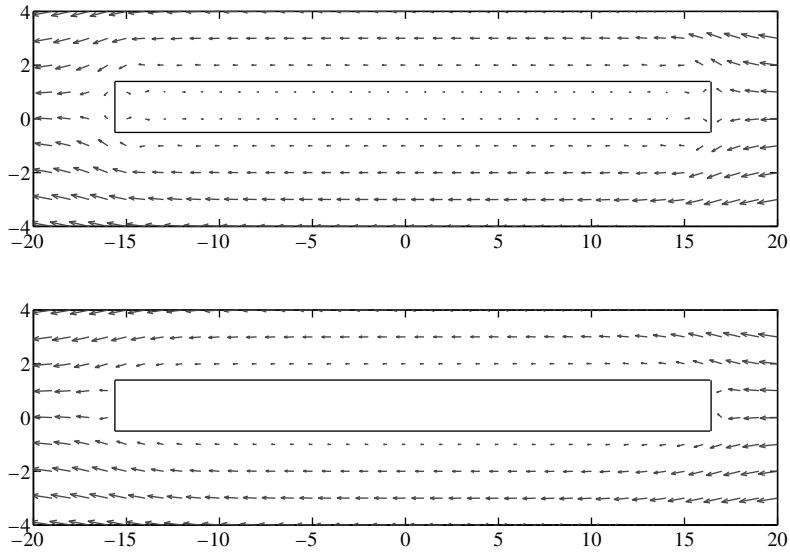
Fig. 11. Top: two-dimensional slice of the three-dimensional velocity field created by a pseudo-cylinder moving in the tangential direction. For clarity, the velocity has been translated so that the pseudo-cylinder is fixed and there is an incoming flow at infinity along the axis of the pseudo-cylinder. The rectangle indicates the effective surface of the pseudo-cylinder. Note that the velocity is nearly zero on the effective surface of the pseudo-cylinder as dictated by the no-slip condition, and that the velocity is small inside the effective surface. Bottom: the slender-body theory approximation to the velocity field of a cylinder of radius r and length $\widetilde{L}$ moving in the tangential direction. The velocity is defined to be identically zero inside the surface of the cylinder. The velocities near the endpoints of the cylinder may not be accurate.
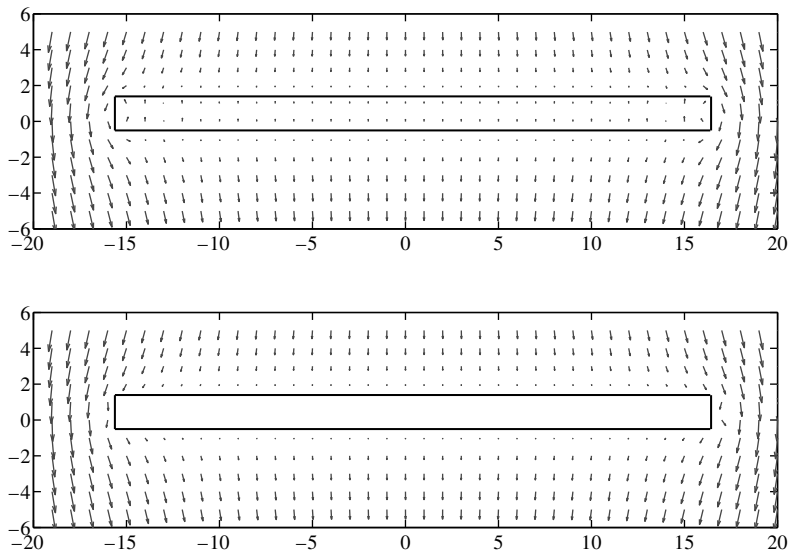
Fig. 12. The velocity field of a pseudo-cylinder (top) and the slender-body theory approximation to the velocity field of a cylinder (bottom) held fixed with an incoming flow in the normal direction from infinity.

interaction of a pseudo-cylinder is close to that of an actual cylinder and is independent of the cylinder's position and orientation. We thus conclude that an array of immersed boundary points that is constrained to move as a rigid body is in fact a good representation of a cylinder in all possible respects.

We have shown that when h is one, a pseudo-cylinder made up of immersed boundary points spaced evenly over a distance L interacts with the fluid like a cylinder of radius $r = \sqrt{2/3}\bar{a}$ and length $\widetilde{L} = L + 2\bar{a}$. When h is
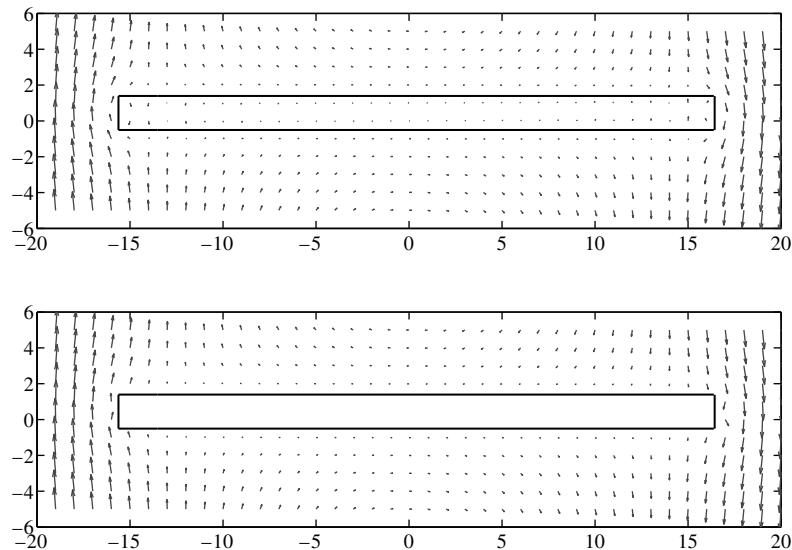
Fig. 13. The velocity field of a pseudo-cylinder (top) and the slender-body theory approximation to the velocity field of a cylinder (bottom) held fixed with an incoming linear shear flow from infinity.

arbitrary, a pseudo-cylinder made up of immersed boundary points spaced evenly over a length L will interact with the fluid like a cylinder of radius $\sqrt{2/3}h\bar{a}$ and length $L + 2h\bar{a}$. The total number of immersed boundary points will scale with h^{-1} if kept at constant density with respect to the grid. If one wishes to represent a rigid cylinder of radius r_C and length L_C by an array of immersed boundary points and one has chosen a delta function and discretization method, then one should first find the effective radius, $\bar{a}$, of a single immersed boundary point that represents a sphere as described above. A cylinder made up of these delta functions will have an effective radius of $\sqrt{2/3}h\bar{a}$, so one should set $h = \sqrt{3/2}r_C/\bar{a}$. One should space the immersed boundary points evenly over a distance $L_C - 2h\bar{a}$, and one should choose a density of points in the preferred range, with two possible good choices being $1.0/h$ and $1/\bar{a}h$. The total number of points will be approximately L_C/h or $L_C/(h\bar{a}) = \sqrt{2/3}L_C/r_C$.
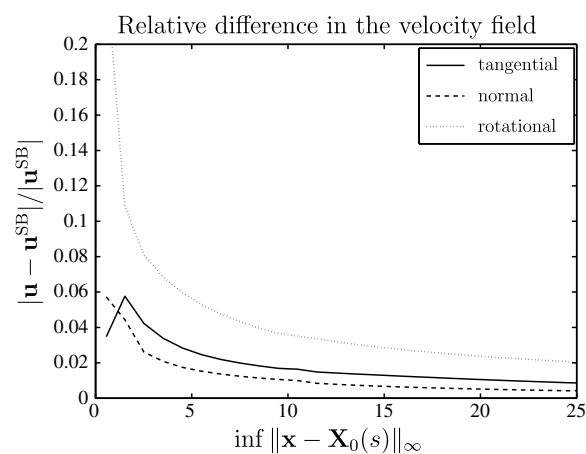
Fig. 14. This plot compares the velocity fields created by a pseudo-cylinder in the immersed boundary method and the slender-body approximation given in Eq. (46). Motion is in the tangential (solid line), normal (dashed line), and rotational (dotted line) directions. We have used δ_4^{IB} and the finite difference discretization. Shown is the relative difference in these fields, plotted against distance from the axis of the cylinder in the infinity norm. These quantities have been averaged in the L_2 sense over rectangular shells of grid points. Even for the worst case, which is rotational motion, the relative difference is 11% at a distance of 1.5 grid cells from the axis of the cylinder, and quickly decays to 2% at a distance of 25 grid cells. For the translational cases, relative difference is small even inside the surface of the cylinder.

Table 1
Reference table of results for the various delta functions and discretization methods used in this paper

Delta function	Finite difference			Spectral			Suggested ρ
	$\bar{a}$	r	$\bar{\epsilon}$	$\bar{a}$	r	$\bar{\epsilon}$	
δ_2^M	0.647	0.528	0.490	0.744	0.607	0.425	1.0
δ_4^M	0.4800	0.3919	0.330	0.5697	0.4651	0.266	1.0
δ_6^M	0.4330	0.3535	0.256	0.5204	0.4249	0.205	1.0
δ_4^D	1.4276	1.1656	0.117	1.4802	1.2085	0.116	$1/\bar{a}$
δ_3^{IB}	0.90678	0.74039	0.0250	0.98666	0.80560	0.0304	1.0
δ_5^{IB}	0.61170	0.49945	0.0137	0.68864	0.56228	0.0164	1.0
δ_4^{IB}	1.25455	1.02433	0.00744	1.31286	1.07194	0.00833	$1/\bar{a}$
δ_6^{IB}	0.77931	0.63631	0.00447	0.84112	0.68677	0.00534	1.0

Shown are the computed effective radius of an immersed boundary point meant to represent a sphere, $\bar{a}$, the inferred effective radius of an array of immersed boundary points meant to represent a cylinder, r, the maximum relative error in the resistance matrix of a point meant to represent a sphere, $\bar{\epsilon}$, and a suggested value for the density of immersed boundary points in an array, ρ. These numbers are computed for the case $h = 1$. The radii, $\bar{a}$ and r, should be scaled by h, and the density, ρ, should be scaled by h^{-1}. Finally, we have found that the effective length of a cylinder represented by an array of immersed boundary points is $2\bar{a}$ plus the extent of the array. Because of smaller errors, we recommend the use of a delta function in the families δ_d^{IB} with d odd or even.

As a reference, we have tabulated in Table 1 the sphere radii, $\bar{a}$, the cylinder radii, r, the maximum error in the resistance matrix of a single point relative to that of a sphere of radius $\bar{a}$, $\bar{\epsilon}$, and a suggested choice of immersed boundary point density, ρ, for the delta functions and discretization methods used in this paper. One should consider the numbers for the radii to be in units of h and the density to be in units of h^{-1}.

5. Conclusion

We have developed a numerical method for immersed boundaries in Stokes flow on an infinite domain that solves the discretized equations using their Green's function. This method allows us to calculate the resistance matrix of a rigid body comprised of an arbitrary configuration of immersed boundary points, as well as the fluid velocity field created by a moving body.

We have applied this method to two simple configurations of immersed boundary points that are commonly used, a single point that is meant to represent a spherical particle, and a linear array of points that is meant to represent a slender cylinder. We have found, in both cases, that with the appropriate choice of parameters, these representations are accurate, and their interactions with the fluid are independent of position and, in the case of the cylinder, independent of orientation with respect to the Eulerian grid.

Our results should be useful to those who perform computations involving spheres and slender bodies in the immersed boundary method, not only because we validate the approach of using a simple, efficient representation, but also because we prescribe specific choices of parameters. The Eulerian grid spacing must be proportional to the physical radius of the spheres or slender bodies simulated and we specify the constants of proportionality for a variety of delta functions in Table 1. The immersed boundary points in an array should have spacing approximately equal to one grid space. If too few or too many points are used, significant dependencies on position and orientation with respect to the Eulerian grid result. Finally, we do not detect a qualitative difference between using a finite difference and a spectral discretization for the the fluid equations, but we have shown that errors are much smaller if the approximate delta functions traditionally used in the immersed boundary method are employed as opposed to higher order delta functions with the same support.

We conjecture that the relative error associated with the representation of a cylinder by an array of immersed boundary points approaches zero in the limit as the aspect ratio, the ratio of the cylinder's length to its radius, goes to infinity. If this turns out to be the case, then the simple representation of a cylinder in the immersed boundary method will be asymptotically accurate in the same way that slender-body theory is asymptotically accurate. Our data so far are inconclusive on this point, and we need to test cylinders of much larger aspect ratios to confirm this conjecture. To do this, we need a more efficient way to compute $\mathcal{S}_1(\mathbf{x})$ for large $|\mathbf{x}|$, and we are currently developing asymptotic methods.

Our numerical method may be used to perform dynamic simulations of rigid or elastic bodies in Stokes flow in an unbounded domain. Used in this way, the method is similar to the method of regularized Stokeslets introduced by Cortez [26,27]. Other methods can perform such simulations for particular types of bodies, such as the Stokesian dynamics method for particles [28] and slender-body theory based methods for rigid or elastic ellipsoids [29,30]. The immersed boundary method can be used for arbitrarily shaped bodies. The computational complexity of our method is proportional to the square of the number of immersed boundary points, which restricts its usefulness. Also the constant of proportionality is large compared to that of the method of regularized Stokeslets, although we can significantly reduce this constant by asymptotic methods that are in current development. A fast algorithm may be possible and is a subject of continuing research. In contrast, the standard immersed boundary method for a finite domain is trivially linear in the number of immersed boundary points.

We conjecture that our results are applicable to representations of spheres and slender bodies in the immersed boundary method at moderate Reynolds number (perhaps as high as ten). Testing this prediction is the subject of future work. The Navier–Stokes equations are nonlinear, and so the relationship of the bodies' velocities to the applied force distribution can be complicated, it is non-trivial to find the constraint force for a rigid body, and we cannot eliminate the fluid variables. Expensive three-dimensional computations are required, and using an unbounded domain is no longer possible. Still, we can study, for instance, numerical solutions of steady Navier–Stokes flow around a single immersed boundary point in a large periodic domain. We can measure the drag on the immersed boundary point as functions of its position in a grid box and its Reynolds number and compare with results for steady flow around a sphere. We conjecture that, at moderate Reynolds number, an immersed boundary point's interactions with the fluid approximate those of a sphere of radius $\bar{a}$, independent of the point's location with respect to the grid.

In any computation using the immersed boundary method, one might question whether the results depend on the position and orientation of the Lagrangian mesh of immersed boundary points relative to the Eulerian fluid grid. Our results show that even for a single immersed boundary point or for a one-dimensional array of points in three dimensions with the proper spacing, such grid effects are small. It seems probable that a more complicated elastic body composed of many immersed boundary points would have even less grid dependence because of averaging. Our results would then indicate that grid dependent effects in the immersed boundary method for the Stokes equations are smaller than may be suspected.

Acknowledgements

Appendix

All delta functions we use are of the following form

$$\delta_h(\mathbf{x}) = \frac{1}{h^3} \phi(x/h)\phi(y/h)\phi(z/h)$$

This appendix includes formulas for the ϕ used to construct the delta functions that appear in this paper. For references, see Section 2.2. Our notational conventions for ϕ are the same as those for δ_h. For example ϕ_2^{M} corresponds to $\delta_{2,h}^{\mathrm{M}}$.

The first family of delta functions provides the maximum possible order of interpolation. We use the first three functions in this family. The formulas for the corresponding ϕ are:

$$\phi_2^{\mathrm{M}}(x) = \begin{cases} 1 - |x| & 0 \leqslant |x| \leqslant 1 \\ 0 & 1 < |x| \end{cases} \tag{A.1}$$

$$\phi_4^{\mathrm{M}}(x) = \begin{cases} 1 - \frac{1}{2}|x| - |x|^2 + \frac{1}{2}|x|^3 & 0 \leqslant |x| \leqslant 1 \\ 1 - \frac{11}{6}|x| + |x|^2 - \frac{1}{6}|x|^3 & 1 < |x| \leqslant 2 \\ 0 & 2 < |x| \end{cases} \tag{A.2}$$

$$\phi_6^{\mathrm{M}}(x) = \begin{cases} 1 - \frac{1}{3}|x| - \frac{5}{4}|x|^2 + \frac{5}{12}|x|^3 + \frac{1}{4}|x|^4 - \frac{1}{12}|x|^5 & 0 \leqslant |x| \leqslant 1 \\ 1 - \frac{13}{12}|x| - \frac{5}{8}|x|^2 + \frac{25}{24}|x|^3 - \frac{3}{8}|x|^4 + \frac{1}{24}|x|^5 & 1 < |x| \leqslant 2 \\ 1 - \frac{137}{60}|x| + \frac{15}{8}|x|^2 - \frac{17}{24}|x|^3 + \frac{1}{8}|x|^4 - \frac{1}{120}|x|^5 & 2 < |x| \leqslant 3 \\ 0 & 3 < |x| \end{cases} \tag{A.3}$$

Plots of these functions are shown in Fig. A.1.

The second family of delta functions satisfies the sum of squares condition (Eq. (22)), but not the balanced condition (Eq. (23)). We use the first two functions in this family. The formulas for the corresponding ϕ are:

$$\phi_3^{\mathrm{IB}}(x) = \begin{cases} 1 + \sqrt{1 - 3|x|^2} & 0 \leqslant |x| \leqslant \frac{1}{2} \\ 5 - 3|x| - \sqrt{-2 + 6|x| - 3|x|^2} & \frac{1}{2} < |x| \leqslant \frac{3}{2} \\ 0 & \frac{3}{2} < |x| \end{cases} \tag{A.4}$$

$$\phi_5^{\mathrm{IB}}(x) = \begin{cases} \frac{17}{35} - \frac{1}{7}|x|^2 + \sqrt{\frac{3123}{39200} - \frac{311}{980}|x|^2 + \frac{101}{490}|x|^4 - \frac{1}{28}|x|^6} & 0 \leqslant |x| \leqslant \frac{1}{2} \\ 1 + \frac{1}{6}|x| - \frac{2}{3}|x|^2 + \frac{1}{6}|x|^3 - \frac{2}{3}\phi_5^{\mathrm{IB}}(|x| - 1) & \frac{1}{2} < |x| \leqslant \frac{3}{2} \\ 1 - \frac{19}{12}|x| + \frac{2}{3}|x|^2 - \frac{1}{12}|x|^3 + \frac{1}{6}\phi_5^{\mathrm{IB}}(|x| - 2) & \frac{3}{2} < |x| \leqslant \frac{5}{2} \\ 0 & \frac{5}{2} < |x| \end{cases} \tag{A.5}$$

The third family of delta functions satisfies the sum of squares condition (Eq. (22)) and the balanced condition (Eq. (23)). We use the first two functions in this family. The formulas for the corresponding ϕ are:

$$\phi_4^{\mathrm{IB}}(x) = \begin{cases} \frac{1}{8}\left(3 - 2|x| + \sqrt{1 + 4|x| - 4|x|^2}\right) & 0 \leqslant |x| \leqslant 1 \\ \frac{1}{8}\left(5 - 2|x| - \sqrt{-7 + 12|x| - 4|x|^2}\right) & 1 < |x| \leqslant 2 \\ 0 & 2 < |x| \end{cases} \tag{A.6}$$

$$\phi_6^{\mathrm{IB}}(x) = \begin{cases} \frac{61}{112} - \frac{11}{42}|x| - \frac{11}{56}|x|^2 + \frac{1}{12}|x|^3 + \frac{\sqrt{3}}{336}(243 + 1584|x| \\ \quad -748|x|^2 - 1560|x|^3 + 500|x|^4 + 336|x|^5 - 112|x|^6)^{\frac{1}{2}} & 0 \leqslant |x| \leqslant 1 \\ \frac{21}{16} + \frac{7}{12}|x| - \frac{7}{8}|x|^2 + \frac{1}{6}|x|^3 - \frac{3}{2}\phi_6^{\mathrm{IB}}(|x| - 1) & 1 < |x| \leqslant 2 \\ \frac{9}{8} - \frac{23}{12}|x| + \frac{3}{4}|x|^2 - \frac{1}{12}|x|^3 + \frac{1}{2}\phi_6^{\mathrm{IB}}(|x| - 2) & 2 < |x| \leqslant 3 \\ 0 & 3 < |x| \end{cases} \tag{A.7}$$
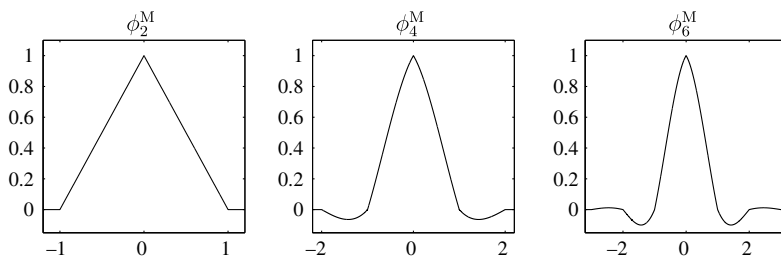
Fig. A.1. Plot of ϕ with maximum moment order.
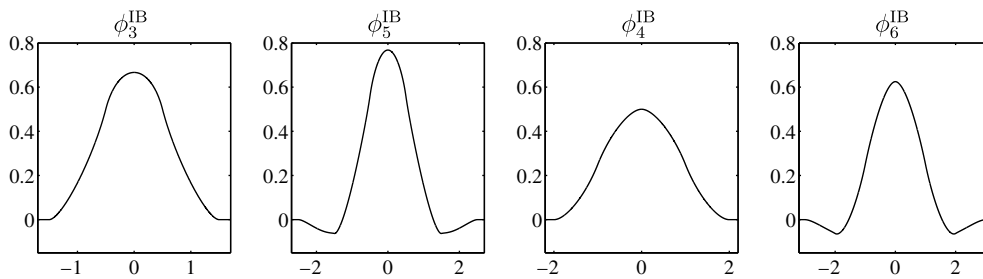
Fig. A.2. Plot of ϕ traditionally used in the immersed boundary method.

Plots of these functions are shown in Fig. A.2.

Finally, we used a scaled and dilated version of $\delta_{2,h}^{\mathrm{M}}$ called $\delta_{4,h}^{\mathrm{D}}$. To define this function we let $\phi_4^{\mathrm{D}}(x) = \phi_2^{\mathrm{M}}(x/2)/2$.

References

[1] C.S. Peskin, D.M. McQueen, Fluid dynamics of the heart and its valves, in: H.G. Othmer, F.R. Adler, M.A. Lewis, J.C. Dallon (Eds.), Case Studies in Mathematical Modeling: Ecology, Physiology, and Cell Biology, Prentice-Hall, Englewood Cliffs, NJ, 1996, pp. 309–337.

[2] D.M. McQueen, C.S. Peskin, A three-dimensional computer model of the human heart for studying cardiac fluid dynamics, Comput. Graph. 34 (1) (2000) 56–60.

[3] M.-C. Lai, C.S. Peskin, An immersed boundary method with formal second-order accuracy and reduced numerical viscosity, J. Comput. Phys. 160 (2) (2000) 705–719.

[4] C.S. Peskin, The immersed boundary method, Acta Numer. 11 (2002) 479–517.

[5] E. Jung, C.S. Peskin, Two-dimensional simulations of valveless pumping using the immersed boundary method, SIAM J. Sci. Comput. 23 (1) (2001) 19–45.

[6] L.A. Miller, C.S. Peskin, A computational fluid dynamics of 'clap and fling' in the smallest insects, J. Exp. Biol. 208 (2) (2005) 195–212.

[7] R. Dillon, L.J. Fauci, D. Gaver, A microscale model of bacterial swimming, chemotaxis and substrate transport, J. Theor. Biol. 177 (4) (1995) 325–340.

[8] D. Bottino, L. Fauci, A computational model of ameboid deformation and locomotion, Eur. Biophys. J. 27 (5) (1998) 532–539.

[9] R. Dillon, L.J. Fauci, An integrative model of internal axoneme mechanics and external fluid dynamics in ciliary beating, J. Theor. Biol. 207 (2000) 415–430.

[10] S. Lim, C.S. Peskin, Simulations of the whirling instability by the immersed boundary method, SIAM J. Sci. Comput. 25 (6) (2004) 2066–2083.

[11] A.L. Fogelson, C.S. Peskin, A fast numerical method for solving the three-dimensional Stokes equations in the presence of suspended particles, J. Comput. Phys. 79 (1) (1988) 50–69.

[12] J.M. Stockie, B.R. Wetton, Stability analysis for the immersed fiber problem, SIAM J. Appl. Math. 55 (6) (1995) 1577–1591.

[13] J.M. Stockie, S.I. Green, Simulating the motion of flexible pulp fibres using the immersed boundary method, J. Comput. Phys. 147 (1998) 147–165.

[14] L.J. Fauci, C.S. Peskin, A computational model of aquatic animal locomotion, J. Comput. Phys. 77 (1) (1988) 85–108.

[15] L. Zhu, C.S. Peskin, Simulation of a flapping flexible filament in a flowing soap film by the immersed boundary method, J. Comput. Phys. 179 (2) (2002) 452–468.

[16] P.J. Atzberger, P.R. Kramer, C.S. Peskin, A stochastic immersed boundary method for biological fluid dynamics at microscopic length scales, J. Comput. Phys. 224 (2) (2007) 1255–1292.

[17] A.-K. Tornberg, B. Engquist, Numerical approximations of singular source terms in differential equations, J. Comput. Phys. 200 (2) (2004) 462–488.

[18] A.M. Roma, C.S. Peskin, M.J. Berger, An adaptive version of the immersed boundary method, J. Comput. Phys. 153 (2) (1999) 509–534.

[19] J. Stockie, Analysis and computation of immersed boundaries, with application to pulp fibres, Ph.D. thesis, University of British Columbia, 1998.

[20] L.G. Ixaru, B. Paternoster, A Gauss quadrature rule for oscillatory integrands, Comput. Phys. Commun. 133 (2) (2001) 177–188.

[21] G.K. Batchelor, An Introduction to Fluid Dynamics, Cambridge University, Cambridge, 2000.

[22] J.B. Keller, S.I. Rubinow, Slender-body theory for slow viscous flow, J. Fluid Mech. 75 (1976) 705–714.

[23] R.E. Johnson, An improved slender-body theory for Stokes flow, J. Fluid Mech. 99 (1980) 411–431.

[24] T. Götz, Interactions of fibers and flow: asymptotics, theory and numerics, Ph.D. thesis, University of Kaiserslautern, 2000.

[25] J. Garcia de la Torre, V.A. Bloomfield, Hydrodynamic properties of complex, rigid, biological macromolecules: theory and applications, Q. Rev. Biophys. 14 (1) (1981) 81–139.

[26] R. Cortez, The method of regularized Stokeslets, SIAM J. Sci. Comput. 23 (4) (2002) 1204–1225.

[27] R. Cortez, L. Fauci, A. Medovikov, The method of regularized Stokeslets in three dimensions: analysis, validation, and application to helical swimming, Phys. Fluids 17 (3) (2005) 31504.

[28] J. Brady, G. Bossis, Stokesian dynamics, Annu. Rev. Fluid Mech. 20 (1) (1988) 111–157.

[29] M.J. Shelley, T. Ueda, The Stokesian hydrodynamics of flexing, stretching filaments, Physica D 146 (1–4) (2000) 221–245.

[30] A.-K. Tornberg, M.J. Shelley, Simulating the dynamics and interactions of flexible fibers in Stokes flows, J. Comput. Phys. 196 (1) (2004) 8–40.